



1 **The new Passive microwave Neural network Precipitation Retrieval (PNPR)**  
2 **algorithm for the cross-track scanning ATMS radiometer: description and**  
3 **verification study over Europe and Africa using GPM and TRMM spaceborne**  
4 **radars**

5  
6 Paolo Sanò<sup>1</sup>, Giulia Panegrossi<sup>1</sup>, Daniele Casella<sup>1</sup>, Anna Cinzia Marra<sup>1</sup>, Francesco Di Paola<sup>2</sup>, Stefano  
7 Dietrich<sup>1</sup>

8  
9 <sup>1</sup> Institute of Atmospheric Sciences and Climate (ISAC), National Research Council of Italy (CNR), 00133 Rome,  
10 Italy

11 <sup>2</sup> Institute of Methodologies for Environmental Analysis (IMAA), Italian National Research Council of Italy (CNR),  
12 C.da S.Loja, Tito Scalo, 85050 Potenza, Italy

13  
14 *Correspondence to:* Paolo Sanò ([paolo.sano@artov.isac.cnr.it](mailto:paolo.sano@artov.isac.cnr.it))  
15  
16  
17  
18  
19  
20  
21  
22  
23  
24  
25  
26  
27  
28  
29  
30  
31  
32  
33  
34  
35  
36  
37  
38  
39  
40  
41  
42  
43  
44  
45  
46  
47  
48  
49  
50  
51  
52  
53  
54  
55  
56



1 **Abstract.** The objective of this paper is to describe the development and evaluate the performance  
2 of a totally new version of the Passive microwave Neural network Precipitation Retrieval (PNPR  
3 v2), an algorithm based on a neural network approach, designed to retrieve the instantaneous  
4 surface precipitation rate using the cross-track ATMS radiometer measurements. This algorithm,  
5 developed within the EUMETSAT H-SAF program, represents an evolution of the previous version  
6 (PNPR v1), developed for AMSU/MHS radiometers (and used and distributed operationally within  
7 H-SAF), with improvements aimed at exploiting the new precipitation sensing capabilities of  
8 ATMS with respect to AMSU/MHS. In the design of the neural network the new ATMS channels  
9 compared to AMSU/MHS, and their combinations, including the brightness temperature differences  
10 in the water vapor absorption band, around 183 GHz, are considered. The algorithm is based on a  
11 single neural network, for all types of surface background, trained using a large database based on  
12 94 cloud-resolving model simulations over the European and the African areas.

13 The performance of PNPR v2 has been evaluated through an intercomparison of the instantaneous  
14 precipitation estimates with co-located estimates from the TRMM Precipitation Radar (TRMM-PR)  
15 and from the GPM Core Observatory Ku-band Precipitation Radar (GPM-KuPR). In the  
16 comparison with TRMM-PR, over the African area, the statistical analysis was carried out for a  
17 two-year (2013-2014) dataset of coincident observations, over a regular grid at  $0.5^\circ \times 0.5^\circ$   
18 resolution. The results have shown a good agreement between PNPR v2 and TRMM-PR for the  
19 different surface types. The correlation coefficient (CC) was equal to 0.69 over ocean and 0.71 over  
20 vegetated land (lower values were obtained over arid land and coast), and the root mean squared  
21 error (RMSE) was equal to  $1.30 \text{ mm h}^{-1}$  over ocean and  $1.11 \text{ mm h}^{-1}$  over vegetated land. The  
22 results showed a slight tendency to underestimate moderate to high precipitation, mostly over land,  
23 and overestimate moderate to light precipitation over ocean. Similar results were obtained for the  
24 comparison with GPM-KuPR over the European area (15 months, from March 2014 to May 2015  
25 of coincident overpasses) with slightly lower CC (0.59 over vegetated land and 0.57 over ocean)  
26 and RMSE ( $0.82 \text{ mm h}^{-1}$  over vegetated land and  $0.71 \text{ mm h}^{-1}$  over ocean), confirming a good  
27 agreement also between PNPR v2 and GPM-KuPR. The performance of PNPR v2 over the African  
28 area was also compared to that of PNPR v1. PNPR v2 has higher R over the different surfaces, with  
29 general better estimate of low precipitation, mostly over ocean, thanks to improvements in the  
30 design of the neural network and also to the improved capabilities of ATMS compared to  
31 AMSU/MHS. Both versions of PNPR algorithm have shown a general consistency with the  
32 TRMM-PR.

33  
34  
35  
36  
37  
38  
39  
40  
41  
42  
43  
44  
45  
46  
47  
48  
49  
50  
51  
52  
53



## 1 **1. Introduction**

2 The availability of data from the Advanced Technology Microwave Sounder (ATMS), a cross-track  
3 scanning radiometer currently onboard the Suomi National Polar-orbiting Partnership (Suomi NPP)  
4 satellite (and on the Joint Polar Satellite System (JPSS) series starting in 2017), represents an  
5 important step in short and long-term weather forecasting and environmental monitoring.  
6 Combining the capabilities of its predecessor sounders such as the Advanced Microwave Sounding  
7 Unit-A (AMSU-A) and the Microwave Humidity Sounder (MHS) aboard NOAA-18 and NOAA-19  
8 and the ESA MetOp-A and MetOp-B satellites, ATMS provides sounding observations with  
9 improved resolution, sampling and coverage for retrieving atmospheric vertical temperature and  
10 humidity profiles. Moreover, this new-generation instrument provides more information about  
11 surface, vertical distribution of hydrometeors, precipitation, and other key environmental variables  
12 (Chen et al., 2007; Boukabara et al., 2013; Zou et al., 2013; Kongoli et al., 2015).

13 With regard to precipitation it should be mentioned that, although the reliable knowledge of its  
14 intensity and accumulation is essential for understanding the global hydrological and energy cycles,  
15 precipitation estimate (from satellite and from the surface) is complicated by several factors: the  
16 large variability of the precipitation in time and space, the conversion of satellite measurements into  
17 quantitative precipitation estimates, uncertainties associated to rain gauges (and to their spatial  
18 distribution), and radar measurements (i.e., attenuation, beam-blocking) and their unavailability in  
19 several regions in the world and over ocean (Mugnai et al., 1993; Iturbide-Sanchez et al., 2011;  
20 Bennartz and Petty, 2001; Tian et al., 2009; Kirstetter et al., 2012).

21 An important step forward towards the improvement of global precipitation monitoring is  
22 represented by the Global Precipitation Measurement (GPM) mission launched on 27 February  
23 2014. GPM is expected to provide accurate precipitation estimates thanks to the availability of the  
24 NASA/JAXA GPM Core Observatory (GPM-CO) [equipped with the GPM Microwave Imager  
25 (GMI) and the Dual-frequency Precipitation Radar (DPR)], a common, global observatory of 3-D  
26 precipitation structure at 5 km resolution, and thanks to the exploitation of a constellation of  
27 international Low Earth Orbit (LEO) satellites equipped with microwave radiometers for  
28 precipitation observation, providing frequent measurements over most of the globe (3-hourly  
29 coverage between 65° S and 65° N) (Hou et al., 2014; Draper et al. 2014; Newell et al., 2014;  
30 Petkovic and Kummerow, 2015). A contribution of ATMS as part of the GPM constellation is  
31 foreseen in this direction, also in relation to the technological improvements over its predecessor  
32 sounders.

33 In Europe, the EUMETSAT “Satellite Application Facility on Support to Operational Hydrology  
34 and Water Management” (H-SAF, Mugnai et al., 2013a), has been called upon to participate in and  
35 to contribute towards the GPM by providing its own precipitation products, and being at the same  
36 time a user of GPM data and a direct collaborator of GPM on two main aspects: development and  
37 refinement of retrieval techniques through the exploitation of all available radiometers in the GPM  
38 constellation, and validation activity. In this context, operational passive microwave (PMW)  
39 precipitation products for the different radiometers are being released within H-SAF as new  
40 radiometers become available, and they are based on two approaches (Mugnai et al., 2013b): the  
41 physically-based Bayesian Cloud Dynamics and Radiation Database (CDRD) algorithm (Casella et  
42 al., 2013, Sanò et al., 2013,) for conically scanning radiometers and the Passive microwave Neural  
43 network Precipitation Retrieval algorithm (PNPR) for cross-track scanning radiometers, originally  
44 developed for AMSU/MHS and fully described in Sanò et al. (2015) (PNPR-AMSU/MHS,  
45 hereafter PNPR v1).

46 The objective of this paper is to describe the development and evaluate the performance of a newly  
47 developed version of PNPR designed to retrieve the instantaneous surface precipitation using the  
48 ATMS radiometer data. This algorithm (PNPR-ATMS, hereafter PNPR v2) represents an evolution  
49 of PNPR v1 (used operationally within the EUMETSAT H-SAF) with improvements aimed at  
50 exploiting the new precipitation sensing capabilities of ATMS with respect to AMSU/MHS.



1 Neural Networks (NNs) represent a highly flexible tool alternative to regression and classification  
2 techniques, widely applied in an increasing fields of the meteorological research for their capability  
3 to approximate complex nonlinear and imperfectly known functions (e.g. Liou et al., 1999; Del  
4 Frate and Schiavon, 1999; Shi, 2001; Marzban, 2003; Blackwell and Chen, 2005; Chen et al., 2006;  
5 Krasnopolsky et al., 2008; Shank et al., 2008; Haupt et al., 2009; Aires et al., 2012).  
6 NNs have been used in precipitation retrieval - precipitation being one of the most difficult of all  
7 atmospheric variables to retrieve - considering the opportunities offered by their ability to learn and  
8 generalize (Hsu et al., 1997; Hall et al., 1999; Staelin et al., 1999; Sorooshian et al., 2000; Chen and  
9 Staelin, 2003; Hong et al., 2004; Sussuravadee and Staelin, 2007, 2008a, 2008b, 2009, 2010;  
10 Bellerby, 2007; Krasnopolsky et al., 2008; Leslie et al., 2008; Mahesh et al., 2011). However, it  
11 should be mentioned that the use of NNs involves the training phase with a large representative  
12 database, often obtained from cloud-resolving model simulations. Consequently, the performance of  
13 the network is largely dependent on the completeness and the representativeness of the database and  
14 on its consistency with the observations.

15 Retrieval algorithms based on NNs, proposed for precipitation estimation from remotely sensed  
16 information, using MW or VIS/IR measurements, are different from each other in the different  
17 approaches used, in the design of the network architecture, in the selection of type and number of  
18 input variables, in the determination of the number of networks used, in the implementation of the  
19 training database (e.g. the cloud-resolving model) and in the training process. With regard to the  
20 input variables, when MW radiometers are used, their choice is normally based on physical  
21 considerations on the radiometric signatures (or brightness temperatures, TBs) of different  
22 microwave channels and on the direct or indirect relationship of these signatures with  
23 environmental, meteorological and microphysical variables (e.g. atmospheric temperature and  
24 humidity, surface conditions, hydrometeor types, size and shapes) involved in the precipitation  
25 retrieval process. The TBs at the MW channels so identified are selected as part of the input  
26 variables. However, some techniques such as principal component analysis (PCA) are applied to the  
27 selected channels in order to reduce the number of inputs, and reduce the complexity of the NN, and  
28 also to reduce the noise (e.g., to filter out the signal due to the background surface), (Chen and  
29 Staelin, 2003; Surussavadee and Staelin, 2008a, 2010; Blackwell and Chen, 2005). Special  
30 functions of TBs, already proposed for rainfall retrieval (Kidd, 1998; Ferraro and Marks, 1995;  
31 Grody, 1991), as the Polarization Corrected Temperature ( $PCT_{85}$ ) or the Scattering Index have also  
32 been considered as the NN inputs (Sarma et al., 2008; Mahesh et al., 2011). Some geographical and  
33 meteorological parameters (e.g. surface type, surface height, season, latitude) are often considered  
34 as auxiliary input data, in order to reduce the ambiguity intrinsic to the PMW precipitation retrievals  
35 based only on observed TBs (e.g., Panegrossi et al., 1998; Kummerow et al., 2011; You and Liou,  
36 2012; You et al., 2015).

37 In the VIS/IR based NN algorithms the input selection is based on different considerations, due to  
38 the indirect relationship between cloud top radiances and surface rainfall and the lack of  
39 information on the precipitation structure within the cloud. Additional inputs are then considered in  
40 addition to TBs, that is, clouds texture information (TB mean and variance for 3x3 and 5x5 pixel  
41 rectangles around each measurement), the rate of change of cloud-top temperatures, the number of  
42 pixels with TB less than a given threshold (Hsu et al., 1997; Bellerby et al., 2000; Tapiador et al.,  
43 2004). This approach normally involves the use of more complex networks.

44 The number of NNs used in the precipitation retrieval algorithms, is defined so as to optimize the  
45 network performance under different operating conditions. In PMW precipitation retrieval separate  
46 NN algorithms are usually proposed depending on the type of surface (i.e., land or sea), to  
47 discriminate between the different precipitation emission signatures relative to background (e.g.  
48 Surussavadee and Staelin, 2008a). Separate NN algorithms are also proposed to deal separately with  
49 stratiform and convective precipitation (e.g. Sarma et al., 2008).



1 In the design of PNPR v2 important aspects in relation to the topics mentioned above, concerning  
2 the choice of the inputs, the number of networks used by the algorithm, and the database used in the  
3 training phase, have been thoroughly analyzed and will be presented in this paper.  
4 Another important issue to consider is that PNPR v2 has been designed in the perspective of the full  
5 exploitation of the MW radiometers in the GPM constellation of satellites, and of the achievement  
6 of consistency (besides accuracy) of the retrievals from the different sensors. These goals are  
7 considered priorities in the international GPM mission community because their achievement leads  
8 to a significant reduction of the errors, also associated with the inadequate sampling of  
9 precipitation, with positive impact on precipitation monitoring (see also Panegrossi et al., 2016),  
10 hydrological applications, and climate studies. This is also true when higher spatial/temporal  
11 resolution products based on MW/IR combined techniques are used, such as IMERG (GPM),  
12 TMPA (Tropical Rainfall Measuring Mission - TRMM), see Huffman et al. (2007, 2015), and also  
13 within the EUMETSAT H-SAF program, these aspects have become a priority. Therefore, PNPR  
14 v2 for ATMS, as well as PNPR v1 for AMSU/MHS, as well as all other H-SAF products for  
15 conically scanning radiometers, represent an important contribution towards the exploitation of the  
16 current and future constellation of PMW radiometers for global precipitation monitoring.  
17 In this paper the PNPR v2 algorithm is described in detail, and the methodology and the results of  
18 an intercomparison of the PNPR v2 instantaneous precipitation estimates with co-located  
19 spaceborne radar estimates from the TRMM Precipitation Radar (TRMM-PR) and from the GPM-  
20 CO Ku-band Precipitation Radar (GPM-KuPR) are presented.  
21 Section 2 presents a brief description of the characteristics of ATMS. In Section 3 a description of  
22 the PNPR v2 algorithm is presented, with reference to the design of the neural network, the main  
23 characteristics of the algorithm, and the relevant features of the ATMS training database. The  
24 verification study is presented in Section 4, which includes a brief description of the characteristics  
25 of PR and DPR, of the methodology used to create the co-located observation dataset used in the  
26 study, the analysis of the performance of PNPR v2 compared to TRMM-PR and to GPM-KuPR,  
27 and a comparison with PNPR v1 using TRMM-PR rainfall estimates as reference. Section 5  
28 contains the conclusive remarks about the performance of PNPR v2 and future perspectives.

29

## 30 **2. The ATMS radiometer**

31 ATMS is a total power cross-track scanning microwave radiometer on board the Suomi National  
32 Polar-orbiting Partnership (NPP) satellite (and JPSS satellites scheduled for early 2017), with a  
33 swath of 2600 km, angular span of  $\pm 52.77^\circ$  relative to nadir (Boukabara et al., 2011, 2013; Weng et  
34 al., 2012; Goldberg et al., 2013; Zou et al. 2013). During each scan the Earth is viewed at 96  
35 different angles, with a spatial sampling of  $1.11^\circ$ . ATMS has 22 channels, ranging from 23 to 183  
36 GHz, providing both temperature soundings from the surface to the upper stratosphere (about 1 hPa,  
37  $\sim 45$  km), and humidity soundings from the surface to upper troposphere (about 200 hPa,  $\sim 15$  km).  
38 Particularly, ATMS channels 1–16 provide measurements at microwave frequencies below 60 GHz  
39 and in an oxygen absorption band, and channel 17–22 are located at higher microwave frequencies  
40 above 89 GHz and in a water vapor absorption band. The beamwidth changes with frequency and  
41 is  $5.2^\circ$  for channels 1-2 (23.8-31.4 GHz),  $2.2^\circ$  for channels 3-16 (50.3 - 57.29 GHz and 88.2 GHz),  
42 and  $1.1^\circ$  for channels 17-22 (165.5-183.3 GHz). The corresponding nadir resolutions are 74.78 km,  
43 31.64 km and 15.82 km respectively. The outmost FOV sizes are 323.1 km x 141.8 km (cross-track  
44 x along-track), 136.7 km x 60.0 km, 68.4 km x 30.0 km, respectively.

45 Compared with its predecessors AMSU and MHS, ATMS has improved resolution (31.6 km at  
46 nadir in the 54 GHz band, vs 48.6 km for AMSU) and spatial sampling ( $1.11^\circ$  in the 54 GHz band,  
47 vs  $3.33^\circ$  for AMSU) and has the great advantages of a wider swath that practically eliminates the  
48 orbital gaps. There are slight differences in the frequencies of ATMS channels 88.2 GHz, 165.5  
49 GHz and  $183.31 \pm 7.0$  GHz with respect to the corresponding MHS channels (89.0 GHz, 157.0 GHz  
50 and 190.31 GHz). Three new channels are added compared to AMSU/MHS: channel 4 (51.76 GHz)  
51 for lower tropospheric temperature sounding, and the two channels 19 and 21 ( $183.31 \pm 4.5$  GHz and



1 183.31±1.8 GHz) to enhance the moisture profiling performance, improving the vertical resolution,  
2 and potentially very useful also for precipitation (Surussavadee et al., 2012; Weng et al., 2012; Zou  
3 et al., 2013).

### 4 5 **3. The new PNPR algorithm**

#### 6 7 **3.1 Algorithm description**

8 PNPR v2 represents an evolution for ATMS applications, of the previous PNPR v1 algorithm based  
9 on a NN approach, developed at ISAC-CNR for precipitation rate estimation using AMSU/MHS  
10 observations. The full description of PNPR v1 is provided in Sanò et al. (2015), while some  
11 important aspects are reviewed in this paper for completeness.

12 Both versions of PNPR are designed to work over the full Meteosat Second Generation (MSG) disk  
13 area (60°S-75°N, 60°W-60°E). In PNPR v1 the training of the NN was carried out using two  
14 distinct NNs, one for the European/Mediterranean area (Sanò et al., 2015) and one for the African  
15 area (Panegrossi et al., 2014). Each network was designed to work with all types of surface  
16 backgrounds (i.e., land, sea, coast) in order to reduce the discontinuity of precipitation estimates  
17 often found in correspondence with transitions between surfaces with different radiometric  
18 properties. In PNPR v2 one unique NN has been designed, capable of operating on the whole MSG  
19 disk area, regardless of the type of surface and of the geographical area.

20 Another significant aspect in the design of PNPR v1 was the use of the TB differences in the water  
21 vapor absorption band channels at 183 GHz as input to the neural network. Opaque channels around  
22 183 GHz were originally designed to retrieve water vapor profiles due to their different sensitivity  
23 to specific layers of the atmosphere (Wang et al., 1997; Staelin and Chen, 2000; Blackwell and  
24 Chen, 2005). However these channels have shown great potentials for precipitating cloud  
25 characterization and for precipitation retrieval. The different penetration ability of these channels in  
26 the atmosphere can be exploited to analyze the vertical distribution of hydrometeors (Wang et al.,  
27 1989, 1997; Burns et al., 1997; Staelin and Chen, 2000; Ferraro et al., 2005; Hong et al., 2005,  
28 2008; Funatsu et al., 2007, 2009; Laviola and Levizzani, 2011), and to obtain some criteria for the  
29 characterization of precipitation as weak, moderate, strong convective or stratiform, using the TB  
30 differences  $\Delta_{17}$ ,  $\Delta_{13}$ , and  $\Delta_{37}$  (corresponding respectively to the differences between the 183.31±1  
31 GHz and 183.31±7 GHz, 183.31±1 GHz and 183.31±3 GHz, 183.31±3 GHz and 183.31±7 GHz  
32 channels) (e.g., Ferraro, 2004; Qiu et al., 2005). In the design of PNPR v2 we have focused on the  
33 exploitation of the improved technical characteristics of ATMS with respect to AMSU/MHS, with  
34 the analysis of the information carried by two new channels in the 183 GHz water vapor absorption  
35 band (at 183.31±4.5 GHz and 183.31±1.8 GHz) (see Section 3.3 dedicated to the input selection).  
36 As in PNPR v1, a Canonical Correlation Analysis has been carried out to find the linear  
37 combination of TBs of selected channels best correlated with surface precipitation rate.

38 The flow diagram of the PNPR v2 algorithm is substantially the same as that of PNPR v1, described  
39 in detail in Sanò et al. (2015), except for the use of one unique network trained on a database  
40 representative of MSG full disk area (see Section 3.2), and changes in the input selection in the  
41 design of the network (described in Section 3.3). Furthermore, in the preprocessing of the  
42 brightness temperatures, in addition to the decoding of the file format and the quality control of the  
43 input data, the removal of the three outmost pixels along the scan is carried out. Other processing  
44 steps of the algorithm, such as the screening procedure of no-rain pixels, the quality index map  
45 providing indications on areas or conditions where the retrieval is more or less reliable, are  
46 unchanged with respect to those used for the algorithm PNPR v1 (Sanò et al., 2015). In a similar  
47 way, also the new algorithm provides in output, in addition to the precipitation rate (mm/h), the  
48 phase of the precipitation (solid, liquid, mixed or unknown), and the quality index. The PNPR v2  
49 output is provided on a grid corresponding to the ATMS nominal resolution varying from 15.82 km  
50 x 15.82 km / circular at nadir to 68.4 km x 30.0 km / elliptical at scan edge.

51



1

## 2 **3.2 The training database**

3 The training of PNPR v2 was performed using a large cloud-radiation database representative of the  
4 MSG full disk area, built from 94 cloud-resolving model (CRM) simulations of different  
5 precipitation events including 60 simulations over the European/Mediterranean area (Casella et al.,  
6 2013), and 34 simulations over Africa and Southern Atlantic (Panegrossi et al, 2014). The  
7 simulations were carried out using the University of Wisconsin Nonhydrostatic Modeling System  
8 (UW-NMS) (Tripoli, 1992; Tripoli and Smith, 2014a, b)) coupled to a Radiative Transfer Model  
9 (RTM) relating CRM environments to expected top-of-atmosphere PMW TBs of the ATMS  
10 radiometer (see Smith et al., 2013, and Casella et al., 2013 for the details about the cloud model  
11 configuration setup, and Sanò et al., 2015 for AMSU/MHS RTM simulations). Figure 1 shows the  
12 geographical location of the inner domain of the 94 simulations. Simulated events were selected in  
13 order to cover the different seasons and different meteorological situations and precipitation  
14 regimes. Simulations over African and South Atlantic area were chosen also on the basis of the  
15 TRMM-PR observations (in particular the Rain Type flag and the Freezing level height) and on the  
16 basis of different climatic regions in order to cover as much as possible the climatic variability in  
17 the area of interest with a limited number of simulations.

18 The simulated TBs were calculated considering the different ATMS viewing angles and channel  
19 frequencies using the same approach used for AMSU/MHS and described in Sanò et al., 2015. The  
20 database contains more than two million entries for the European/African regions and has 45 views  
21 for each entry (the three outmost pixels were discarded due to the low resolution).

22

## 23 **3.3 Input selection**

24 The first objective in the new NN design was the selection of the inputs based on the evaluation of  
25 their impact on the performance of the NN or on their sensitivity to precipitation. Consistently with  
26 PNPR v1 and on the basis of the results obtained for AMSU/MHS (Sanò et al., 2015), for the new  
27 NN we have initially imposed the use of the three inputs  $\Delta_{17}$ ,  $\Delta_{13}$ , and  $\Delta_{37}$  (Hong et al., 2005;  
28 Funatsu et al., 2007, 2009). These TB differences have been proven to be very effective in detecting  
29 precipitation, differentiating between different precipitation structures and in the retrieval of rainfall  
30 rate. For PNPR v2, a detailed analysis to evaluate the effect of additional inputs on the performance  
31 of the NN has been carried out. All possible TB differences with the two new ATMS 183 GHz  
32 ( $183.31 \pm 1.8$  GHz and  $183.31 \pm 4.5$  GHz) channels were considered, and the analysis was based on a  
33 cross-validation method (Anders and Korn, 1999; Marzban, 2009), already used for PNPR v1 (Sanò  
34 et al., 2015). This method consists, essentially, in comparing the quality of two NNs by evaluating  
35 their mean squared prediction error (MSPE) when they are applied to an equal number (M) of  
36 validation data sets. Therefore, the cross-validation index (CV) is defined as:

37

$$CV = \frac{1}{M} \sum_{m=1}^M MSPE_m$$

38

39 In a first test, only the three differences  $\Delta_{14}$ ,  $\Delta_{24}$ , and  $\Delta_{27}$  (corresponding respectively to the  
40 differences between the  $183.31 \pm 1$  GHz and  $183.31 \pm 4.5$  GHz,  $183.31 \pm 1.8$  GHz and  $183.31 \pm 4.5$   
41 GHz, and  $183.31 \pm 1.8$  GHz and  $183.31 \pm 7$  GHz channels) showed a real improvement in the NN  
42 performance. The use of the differences between contiguous channels resulted in fact irrelevant.  
43 The subsequent tests with these three new inputs proved that  $\Delta_{24}$ , added to  $\Delta_{17}$ ,  $\Delta_{13}$ , and  $\Delta_{37}$  already  
44 selected in PNPR v1, was the input with most significant impact on the NN performance. Table 1  
45 shows some results obtained during the test.

46 In the table the various possible differences considered as input to the NN in this analysis are shown  
47 in the first column;  $\Delta_F = \Delta_{13}, \Delta_{37}, \Delta_{17}$  denotes the three difference combinations used in the PNPR  
48 v1 algorithm. In the second and fourth columns the values of the correlation coefficients between  
49 output and target during the learning phase ( $R_L$ ), and the mean values during the cross-validation



1 phase ( $R_{CV}$ ) are shown. In the third and the fifth columns the values of the mean squared error  
2 during the learning phase ( $MSE_L$ ), and the cross-validation index CV (the mean MSPE values  
3 during the cross-validation phase) are provided. From the results shown in the table it is evident that  
4 the NN performance improves when the input  $\Delta_{24}$  is added. It is worth noting that to achieve the  
5 results shown in Table 1 the training protocol described in Sanò et al. (2015) has been applied, and  
6 that for each input configuration (each row in the table) more than one hundred NNs (with different  
7 levels of perceptrons) were compared to select the optimal network configuration.

8 The contribution of  $\Delta_{24}$  as new input can be seen as a compensation of  $\Delta_{17}$  when, under certain  
9 conditions, this is affected by the “noise” of the background surface. In fact, the  $183\pm 7$  GHz  
10 channel, the most penetrating among the 183 GHz channels, has a weighting function peaking at the  
11 lowest levels (Bennartz and Bauer, 2003), and the TB can be significantly affected by the signal  
12 from the underlying surface (for example in cold and dry conditions). On the other hand, in the  
13 same conditions, the  $183\pm 4.5$  GHz channel has a weighting function peaking at higher levels. Some  
14 tests have been carried out on different cloud model profiles extracted from the CRM simulations  
15 and based on RTM computations to analyze the behavior of the  $\Delta_{17}$  and  $\Delta_{24}$ , and they have  
16 confirmed these effects (not shown). We have also verified that, by replacing  $\Delta_{17}$  with  $\Delta_{24}$ , a lower  
17 performance of the network is achieved, whereas the combined use of the two differences  
18 guarantees the optimal performance. The use of  $\Delta_{24}$  as added input to  $\Delta_{17}$ ,  $\Delta_{13}$ , and  $\Delta_{37}$  in PNPR v2  
19 represents the best compromise between the achievement of a good performance and the  
20 minimization of the number of inputs of the NN in order to reduce its complexity, key aspects in  
21 any NN design.

22 Another difference between PNPR v2 and PNPR v1 algorithms is the result of the canonical  
23 correlation analysis (CCA) applied to the training database to find the linear combination of TBs  
24 (LCT) of selected channels best correlated with surface precipitation rate, to be used as additional  
25 input to the network (see Sanò et al., 2015). The resulting linear combination for ATMS is  
26 composed of the window channels 31.4 GHz, 88.2 GHz, and 165.5 GHz, showing the highest  
27 correlation coefficients in the CCA analysis (with respect to the surface rain rate) for all types of  
28 background surfaces (in PNPR v1 for AMSU/MHS the 50.3 GHz, 89 GHz, and 150 GHz were  
29 selected for LCT).

30 With regard to other inputs to the network, in PNPR v2 the same ancillary data used in PNPR v1  
31 were maintained (surface height, background surface type, month, and secant of the zenith angle  
32 along the ATMS cross-track scan). An additional auxiliary input was added to drive NN in the  
33 transition between the European and African area, i.e., the monthly mean total precipitable water  
34 (TPW) obtained from ECMWF Era Interim reanalysis in the 2011-2014 period. It should be  
35 mentioned that the use of geographical and environmental/meteorological parameters (including  
36 TPW) in PMW precipitation retrieval is utilized to reduce the ambiguity intrinsic to the PMW  
37 precipitation retrieval process (for example in the NASA GPM Bayesian algorithms - see  
38 Kummerow et al., 2011, 2015; Kidd et al., 2016).

39 During the phase of network design and the training process, more than 400 architectures have been  
40 tested and an optimal NN has been obtained, where “optimal” refers to the one with best  
41 performance, i.e., minimum CV over the full dynamic range of the inputs, absence of overfitting,  
42 and absence of anomalous inhomogeneities in the retrievals (Sanò et al., 2015; Staelin and  
43 Surussavadee, 2007).

44 In summary, ten input variables (five TBs derived and five ancillary inputs) are used in the NN for  
45 ATMS:

- 46 1. a linear combination of TBs (LCT) at 31.4, 88.2 and 165.5 GHz;
- 47 2.  $\Delta_{17}$  difference between the TBs of channels  $183.31\pm 1$  and  $183.31\pm 7$  GHz;
- 48 3.  $\Delta_{37}$  difference between the TBs of channels  $183.31\pm 3$  and  $183.31\pm 7$  GHz;
- 49 4.  $\Delta_{13}$  difference between the TBs of channels  $183.31\pm 1$  and  $183.31\pm 3$  GHz;
- 50 5.  $\Delta_{24}$  difference between the TBs of channels  $183.31\pm 1.8$  and  $183.31\pm 4.5$  GHz;
- 51 6. surface type (land, sea, coast);





- 1 7. monthly mean TPW;
- 2 8. month;
- 3 9. surface height (altitude);
- 4 10. secant of the zenith angle.

5 The network architecture is similar to that of PNPR v1, with one input layer (with number of nodes  
 6 equal to the number of inputs) and two hidden layers with 23 and 10 nodes in the first and in the  
 7 second layer respectively (the number of nodes differs from PNPR v1). The tan-sigmoid transfer  
 8 function is used for the input and the hidden layers, while a linear transfer function is used for the  
 9 output node.

10

### 11 3.4 Sensitivity analysis

12 During the training procedure, an assessment of the sensitivity of the NN output to variations of the  
 13 inputs was carried out. Sensitivity analysis provides an estimation of the relative importance of the  
 14 inputs (Coulibaly et al., 2005). The knowledge of the NN behavior, in relation to input perturbation,  
 15 helps to assess the relevance of the individual contributions to the output, and to verify the correct  
 16 training of the NN (i.e., the weights remain stable) that is achieved when there is no significant  
 17 changes of the sensitivity during the last training iterations (epochs).

18 The sensitivity analysis, limited to the TBs derived variables that are more related to the rain rate  
 19 estimate, and not to the ancillary variables, was applied to the "optimal NN" (i.e., defined by the  
 20 listed inputs and the architecture described in the previous section), and was carried out during the  
 21 final phase of the training (see Sanò et al., 2015). The final phase was reached when the two  
 22 parameters indicating the quality of the learning process, i.e. the correlation coefficient (R) and the  
 23 gradient of performance (mean squared error), were respectively larger than 0.89 and less than 0.05,  
 24 with the number of epochs in the 700-900 range (see Sanò et al., 2015 for more details on this  
 25 procedure). The assessment of the sensitivity was carried out several times, in correspondence to  
 26 successive epochs (to ensure the representativeness of the data used for the analysis), and for three  
 27 different surface types (land, coast and ocean), using NN input data randomly extracted from the  
 28 training and test databases. Five inputs ( $\Delta_{13}$ ,  $\Delta_{37}$ ,  $\Delta_{17}$ ,  $\Delta_{24}$ , LCT) were slightly perturbed by  
 29 percentages of their value within three times their standard deviation (calculated in the database).

30 The relative sensitivity (S) of the NN to each input (i.e., for a number of input perturbations) is  
 31 calculated as the ratio between the mean standard deviation of the output (i.e., the surface rainfall  
 32 rate), and the mean standard deviation of the input.

33

$$S_i = \frac{\overline{\sigma(RR_i)}}{\sigma(V_i)}$$

34 where  $S_i$  is the relative sensitivity corresponding to the input  $V_i$  and  $\sigma(RR_i)$  and  $\sigma(V_i)$  are the  
 35 standard deviations of the rainfall rate and the input variable. Figure 2 shows the results obtained  
 36 for the three different background surface types considered.

37 The results show a similar behavior of the sensitivity for the three different surface backgrounds  
 38 considered. It is evident the higher sensitivity of NN with respect to the LCT in comparison with the  
 39 other inputs; this is due to the contribution of window channels used in LCT, selected by  
 40 maximizing the correlation with the surface precipitation rate. Another important aspect is the  
 41 relative contribution of the other inputs (TBs difference in the 183 GHz band channels) quite  
 42 similar among the three types of surface, with a slightly higher contribution of the input  $\Delta_{17}$  for land  
 43 and coast and a good contribution of the new ATMS input  $\Delta_{24}$  for all surface types.

44

## 45 4. Verification study

46

### 47 4.1 Dataset description



1 This section presents the verification study carried out for the PNPR v2 algorithm, using as  
2 reference the data provided by the TRMM and GPM spaceborne radars. The TRMM-PR is a 13.8  
3 GHz radar with a swath width of 247 km (after the satellite was boosted to higher orbit in 2001). Its  
4 coverage allows regional intercomparison of convective–stratiform contributions to precipitation  
5 across the Tropics, with data available since the launch of the satellite in November 1997 until  
6 October 2014. It is considered the precursor to GPM DPR, and has represented, during this time  
7 interval, the best available remote-sensing instrument for precipitation (Schumacher and Houze,  
8 2003). The TRMM PR2A25 product (Iguchi et al. 2000) provides rainfall rates based on the  
9 reflectivity-rainfall rate relationships, along with a raindrop size distribution (DSD) model,  
10 attenuation correction, and a non-uniform beam filling correction. Even though issues have been  
11 raised about the accuracy of PR2A25, related to surface properties, variations of the DSD, or impact  
12 of incidence angles (i.e., Iguchi et al., 2009; Hirose et al., 2012; Kirstetter et al., 2013), during its  
13 operational period this radar has provided accurate estimates of instantaneous rain rate, as well as  
14 calibration for other precipitation-relevant sensors in sun-synchronous orbits (Bellerby et al., 2000;  
15 Heymsfield et al. 2000; Liao et al. 2001; Schumacher and Houze, 2003; Lin and Hou, 2008). The  
16 GPM DPR (on board the GPM-CO) is composed of two precipitation radars, the GPM-KuPR at  
17 13.6 GHz (an updated version of the TRMM-PR), and the Ka-band Precipitation radar (GPM-  
18 KaPR) at 35.5 GHz. The simultaneous use of the two radars was designed to obtain a greater  
19 dynamic range in the measurements, more detailed information on the microphysical rain structure  
20 (such as raindrop size distribution), and a consequent better accuracy in the rainfall retrieval (Le and  
21 Chandrasekar, 2103a, 2013b; Hou et al., 2014; Chandrasekar et al., 2014). KuPR and KaPR have  
22 the same space resolution at nadir, equal to 5.2 km, the same beamwidth, equal to 0.71°, and cross  
23 track swath widths of 245 km and 120 km, respectively. In this study we have considered only the  
24 GPM-KuPR products because of the similarity with the TRMM-PR and because its larger swath  
25 size offers better chances to find coincident observations with ATMS. It is worth considering also  
26 that in spite of the similarity between the two radars, the GPM-KuPR has higher sensitivity (with  
27 minimum detectable reflectivity between 12 dBZ and 14 dBZ, outperforming the original  
28 instrumental design of 18 dBZ) (Toyoshima et al., 2015; Hamada and Takayabu, 2016) than the  
29 TRMM-PR radar (18 dBZ minimum detectable reflectivity).

30 Two datasets have been created, one composed by two years (2013-2014) of coincident Suomi-NPP  
31 ATMS and TRMM-PR overpasses over the African area (36° S - 36° N and 60° E - 30° W), and  
32 one made of 15 months (1 March 2014- 31 May 2015) of ATMS and GPM-KuPR coincident  
33 overpasses over the European and African areas (36° S - 65° N and 60° E - 30° W). In the study the  
34 comparison is carried out between the PNPR v2 precipitation rate and the NASA/JAXA  
35 precipitation products from the two spaceborne radars, in particular the TRMM-PR standard  
36 product 2A25 (V7), and GPM 2ADPR Ku normal scan (Ku-NS) (V03). Coincident observations in  
37 the area of interest within a 15 minute time window have been considered between ATMS and  
38 TRMM-PR (hereafter ATMS-PR) and between ATMS and GPM-Ku-NS (hereafter ATMS-DPR-  
39 Ku).

40 It should be pointed out that the results obtained from the ATMS-DPR-Ku coincidence dataset are  
41 not as robust as the results obtained from the ATMS-PR dataset because of the limited size of the  
42 dataset, and because of some uncertainties in the less consolidated day-1 V03 DPR products, linked  
43 to factors such as the DSD parameterization (Liao et al., 2014), the evaluation of the path-integrated  
44 attenuation (PIA), the surface reference technique (SRT), and the non-uniform beam filling effect  
45 (NUBF) (Shimozuma and Seto, 2015).

46 Figure 3 (left panel) shows the geographical distribution (on the ATMS grid) of about 1.8 millions  
47 coincident pixels ATMS-PR found over the African area in the two-year time frame 2013-2014.  
48 The figure shows a rather good coverage of the entire area, with a number of coincident pixels  
49 between 30 and 150 on Central Africa, increasing moving to the North and to the South.

50 In the right panel of the figure, the distribution of the coincident pixels ATMS-DPR-Ku over the  
51 European and African areas, between March 2014 and May 2015, is shown. In contrast to the left



1 panel, the coverage is not as good with a lower number of coincident pixels, and with some  
2 uncovered areas. The number on coincident pixels increases over northern Europe at the high  
3 latitudes reaching a maximum value around 200. In the southern part of Europe and Africa, the  
4 number of coincidences is significantly reduced (maximum values around 50).  
5 To obtain co-located vectors of rainfall estimates of ATMS and TRMM-PR, and of ATMS and  
6 GPM-KuPR, the radar precipitation rate at the surface was downscaled to the PNPR v2 product  
7 nominal resolution (variable along the scan line, see Section 3.1), by averaging the rainfall rate of  
8 all radar pixels falling within each PNPR v2 pixel. In order to reduce the geolocation and  
9 synchronization errors, due to the different viewing geometry of ATMS and the spaceborne radar,  
10 and to the time lag between the observations, statistical analysis was carried out over a regular grid  
11 at  $0.5^\circ \times 0.5^\circ$  resolution. For some of the analysis the coincidence datasets were categorized on the  
12 basis of the background surface – vegetated land, arid land (for Africa only), ocean, and coast –  
13 using a digital land/sea map at 2s of arc resolution (see Casella et al., 2015).

14

#### 15 4.2 Comparison with TRMM-PR

16 Figure 4 shows the geographical distribution of the values of three statistical indexes (hit bias,  
17 correlation coefficient (CC), and Root Mean Squared Error (RMSE), (see Tian et al. (2016) for the  
18 definition of these scores), obtained for the ATMS-PR dataset. The scores are computed  
19 considering all coincident ATMS-PR pixels within each  $0.5^\circ \times 0.5^\circ$  grid box (regardless of the time  
20 of the overpasses) with precipitation rate greater than  $0 \text{ mm h}^{-1}$  both from the radiometer and the  
21 radar (hits only).

22 The top panel shows a rather uniform distribution of low bias (between  $-0.2$  and  $0.1 \text{ mm h}^{-1}$ ,  
23 negative in most regions), with areas with larger positive bias ( $0.8 \text{ mm h}^{-1}$ ) over the Equatorial  
24 region, mostly over the Atlantic and Indian Ocean, and a few scattered areas of larger negative bias  
25 ( $-0.8 \text{ mm h}^{-1}$ ). Moreover, the algorithm shows an overall good correlation (middle panel) ( $CC > 0.8$   
26 in most areas), and a RMSE (bottom panel) with a pattern quite similar to the hit bias, with most  
27 values between  $0.2$  and  $0.5 \text{ mm h}^{-1}$ , and a limited number of grid points with values around  $1.3 \text{ mm h}^{-1}$ .  
28 Overall, the panels point out a good agreement between PNPR v2 and TRMM-PR, evidenced  
29 by the widespread low values of bias and RMSE and the high values of CC.

30 In Fig. 5 the density scatterplots for all  $0.5^\circ \times 0.5^\circ$  resolution grid-boxes of the ATMS-PR dataset  
31 are shown for different surface types. In the scatterplot, the coordinates are the values (in  
32 logarithmic scale) of the mean precipitation rate from ATMS and for TRMM-PR in each grid-box,  
33 while the color represents the number of points in the dataset for each pair of precipitation rate  
34 values. The correlation is quite good for all background surfaces. A significant number of  
35 coincident observations below the diagonal is found over ocean, mostly for precipitation rates less  
36 than  $1 \text{ mm h}^{-1}$ , and over vegetated land (for all precipitation rates) This confirms the overall slight  
37 underestimation (negative hit bias) over land of Fig. 4 (top panel). The values of the statistical  
38 indexes (hit bias, CC and RMSE) calculated over the entire dataset are also provided, and they  
39 confirm the good agreement between PNPR v2 and TRMM-PR for the different surface types  
40 (results for coast and arid land are affected by the low number of coincident pixels found for these  
41 areas). The (small) bias is negative for vegetated land ( $-0.08 \text{ mm h}^{-1}$ ) and arid land ( $-0.05 \text{ mm h}^{-1}$ ),  
42 and positive for ocean and coast ( $0.05 \text{ mm h}^{-1}$ ). Low RMSE is also found for all surface types,  
43 higher for ocean ( $1.30 \text{ mm h}^{-1}$ ), than for vegetated land ( $1.11 \text{ mm h}^{-1}$ ), and equal to  $0.80$  and  $1.37$   
44  $\text{mm h}^{-1}$  for arid surfaces and coastal area respectively. CC is higher for vegetated land ( $0.71$ ),  
45 compared to ocean ( $0.69$ ), coast ( $0.65$ ) and arid land ( $0.64$ ).

46 Table 2 presents the contingency table for the ATMS-PR dataset, based on the mean rainfall rate  
47 from ATMS and TRMM-PR within each  $0.5^\circ \times 0.5^\circ$  grid-box. The percentages shown in a given  
48 column, provided for the four surface backgrounds, represent how the PNPR v2 product classifies  
49 the precipitation assigned to each TRMM-PR class. Four rainfall rate intervals were selected in this  
50 comparison,  $0.01 - 0.25 \text{ mm h}^{-1}$ ,  $0.25 - 1 \text{ mm h}^{-1}$ ,  $1 - 5 \text{ mm h}^{-1}$  and  $5 - 15 \text{ mm h}^{-1}$ . There is an  
51 appreciable general consistency between PNPR v2 and TRMM-PR estimates, as shown by the



1 largest percentages found on the main diagonal for each type of surface background. The  
2 percentages exceed 70% for low precipitation rates ( $\leq 0.25 \text{ mm h}^{-1}$ ) and 50% for higher  
3 precipitation rates. Looking at the distribution of the percentages for each radar range (in each  
4 column), it is noticeable the underestimation of PNPR v2 compared to TRMM-PR (higher  
5 percentages in the cells above the diagonal), which confirms what shown in Fig. 5, for vegetated  
6 land and ocean.

7 Table 3 shows the Performance Index calculated for the different background surfaces, defined as:

8

$$Perf. Index = 100 * \frac{\sum_{i=1}^4 \frac{n_{ij(i=j)}}{\Delta_i}}{\sum_{i=1}^4 \left( \frac{\sum_{j=1}^4 n_{ij}}{\Delta_i} \right)}$$

9

10 where  $n_{ij}$  is the number of occurrences in cell  $ij$ ,  $i$  is the column index and  $j$  is the row index, and  $\Delta_i$   
11 is the width of the  $i$ -th rain rate class ( $\text{mm h}^{-1}$ ). For each surface type, the index consists of the  
12 weighted sum of the number of occurrences in the main diagonal of the cells, divided by the  
13 weighted sum of the total number of occurrences, where the weight is the rain rate range for each  
14 class. The values shown confirm the good ability of the PNPR v2 to provide precipitation rates  
15 consistently with TRMM-PR, mostly over ocean.

16

17

### 18 4.3 Comparison with GPM-KuPR

19 As mentioned previously, a verification of PNPR v2 algorithm has been made also using  
20 precipitation rate estimates from the GPM-KuPR, available at mid-high latitudes. This was initially  
21 intended for the European area only, where a larger number of coincident overpasses are available  
22 during the time frame considered (March 2014 - May 2015) (see Fig. 3). However, results are  
23 shown also for the African area, despite the lower number of coincidences available, in order to  
24 assess the degree of consistency of the results obtained over the same area with the two Ku-band  
25 spaceborne radars.

26 As for the comparison with the TRMM-PR, all co-located ATMS and GPM-KuPR retrievals were  
27 regridded at a  $0.5^\circ \times 0.5^\circ$  resolution, and only grid-boxes with precipitation rates greater than  $0 \text{ mm}$   
28  $\text{h}^{-1}$  (hits) are considered. In Fig. 6 the density scatterplots over the African area and the European  
29 area are shown, for vegetated land and ocean (the number of coincidences for the other surface  
30 types are too low in the ATMS-DPR-Ku dataset). The corresponding values of bias, CC and RMSE  
31 computed over the whole dataset are also provided in each panel. Over Africa, both panels show  
32 patterns quite similar to those found in the comparison with TRMM-PR (Fig. 5). Also in this case  
33 there is a slight underestimation for low precipitation ( $< 1 \text{ mm h}^{-1}$ ) more evident over the ocean.  
34 Table 4 shows the comparison between statistical indexes obtained for the ATMS-DPR-Ku dataset  
35 and those obtained for the ATMS-PR dataset, shown in Fig. 5.

36 The Table shows a good agreement between the scores obtained with two datasets, with very low  
37 bias (slightly positive/negative over land/ocean for the ATMS-DPR-Ku dataset, while the reverse is  
38 valid for the ATMS-PR dataset), low RMSE (lower for the ATMS-DPR-Ku dataset), and good  
39 correlation.

40 The right panels of Fig. 6 show the scatterplots obtained in the comparison of PNPR v2 and GPM-  
41 KuPR over the European area. Pixels with likely presence of ice or snow on the ground have been  
42 eliminated from the dataset, in order to exclude from the verification study cases of snowfall (or  
43 precipitation over frozen background), whose precipitation rate estimate is affected by larger  
44 uncertainty (both in the GPM-DPR-Ku V03 product and in PNPR). For the identification of these  
45 pixels the "Snow Depth" and "Sea Ice Cover" products from the ECMWF Era Interim re-analysis  
46 (at  $0.5^\circ \times 0.5^\circ$  resolution) available every 6 hours have been used. A dataset corresponding to the  
47 ATMS-DPR-Ku coincidence rainfall pixels has been created, considering the ECMWF re-analysis



1 closest in time to each overpass, and using the nearest-neighbor approach to match the ATMS-  
2 DPR-Ku pixels with the ECMWF grid.  
3 The scatterplots in Fig. 6 show a similar behavior for vegetated land for the two areas, while over  
4 ocean in the European area there is a general tendency of PNPR v2 to overestimate the precipitation  
5 with respect to the GPM-KuPR. The total bias has very low values, negative for vegetated land (-  
6 0.12 mm h<sup>-1</sup>) and positive for ocean (0.12 mm h<sup>-1</sup>). The CC show lower values than for the African  
7 region for the two background surfaces (0.59 for vegetated land, 0.57 for ocean), while the RMSE is  
8 lower than over the African region, equal to 0.82 mm h<sup>-1</sup> for vegetated land, equal to 0.71 mm h<sup>-1</sup>  
9 for ocean.

10 In order to better interpret the results in Fig. 6, the geographical distribution over the European area  
11 of bias, CC and RMSE is shown in Fig. 7 (similarly to Fig. 4). In these maps the statistical indexes  
12 are evaluated including pixels with snow or ice on the ground. There is a prevalence of a positive  
13 bias (although mostly below 0.3 mm h<sup>-1</sup>, with some peaks above 0.5 mm h<sup>-1</sup>) over the ocean (in the  
14 Northern Atlantic Ocean, top-left panel) and in the few areas available in the coincidence dataset  
15 over the Mediterranean Sea. In the remaining areas and over land there is a rather uniform  
16 distribution of lower bias (between -0.2 and 0.2 mm h<sup>-1</sup>). The correlation CC has quite high values  
17 (prevalently between 0.80 and 1) throughout the European area, except for some regions in the  
18 Northern Atlantic Ocean, where the values are around 0.6. The RMSE presents quite similar  
19 patterns as the hit bias, with higher values (around 0.7 mm h<sup>-1</sup> and 1-1.5 mm h<sup>-1</sup> for few pixels)  
20 where the bias is high, and lower values (less than 0.5 mm h<sup>-1</sup>) where the bias is low.

#### 21 22 **4.4 Comparison with PNPR v1**

23 In the second part of the verification study we have compared the performances over the African  
24 area of the PNPR v2 with the PNPR v1., to evaluate whether the use of the new ATMS channels  
25 and the newly designed NN have led to improvements in the retrievals. The performance of the  
26 PNPR v1 algorithm has been tested on the same two years period (2013-2014) used for PNPR v2,  
27 considering coincident observations of AMSU/MHS radiometers, on board the NOAA-18, NOAA-  
28 19, Metop-A and Metop-B satellites, with TRMM-PR. The PNPR v1 and TRMM-PR coincidence  
29 dataset is made of about three million pixels. The procedure used to evaluate the PNPR v1  
30 performance is the same as that adopted for the PNPR v2 algorithm, described in section 4.1.

31 Table 5 presents the values of the statistical indexes hit bias, CC, and RMSE obtained in the  
32 comparison of PNPR v1 and PNPR v2 with TRMM-PR precipitation retrievals, over a 0.5° × 0.5°  
33 regular grid, for different background surfaces. These results indicate a good agreement of both the  
34 algorithm retrievals with the TRMM-PR (NASA/JAXA product 2A25), and a better performance of  
35 PNPR v2 especially over vegetated land, in terms of CC (0.71 for PNPR v2 vs. 0.68 for PNPR v1)  
36 and RMSE (1.11 mm h<sup>-1</sup> vs. 1.65 mm h<sup>-1</sup>), and over ocean in terms of all scores (CC = 0.69 vs. 0.61,  
37 RMSE = 1.30 mm h<sup>-1</sup> vs. 2.32 mm h<sup>-1</sup> and hit Bias = 0.05 mm h<sup>-1</sup> vs. 0.59 mm h<sup>-1</sup>). Over arid land  
38 and coast PNPR v2 results might be affected by the limited size of the ATMS-PR coincidence  
39 dataset (ATMS is on board one satellite only, while AMSU/MHS is on board four different  
40 satellites). Improvements compared to PNPR v1 are evident in terms of hit bias (-0.05 mm h<sup>-1</sup> vs.  
41 0.30 mm h<sup>-1</sup> for arid land, and 0.05 mm h<sup>-1</sup> vs. 0.20 mm h<sup>-1</sup> for coast), and in terms of RMSE (0.80  
42 mm h<sup>-1</sup> vs 1.84 mm h<sup>-1</sup> for arid land, and 1.37 mm h<sup>-1</sup> vs 1.90 mm h<sup>-1</sup> for coast).

43 A further analysis of the performance of the two algorithms has been performed through the study  
44 of the Relative Bias percentage (RB<sub>%</sub>) and the Adjusted Fractional Standard Error Percentage  
45 (AFSE<sub>%</sub>) used to remove systematic errors (Tang et al., 2014), as a function of the mean TRMM-PR  
46 rainfall rate value computed for different rainfall rate intervals (bins). In the analysis we have used  
47 rain rate bins of variable size to obtain a meaningful number of pixels within each bin.

48 These variables are defined as

49

$$Relative\ bias\ \% = 100 * \frac{\sum_{i=1}^N (mw_i - rr_i)}{\sum_{i=1}^N rr_i}$$



1

$$\text{Adjusted FSE}\% = \frac{\sqrt{\frac{1}{N} \sum_{i=1}^N (mw_i - rr_i - bias)^2}}{\frac{1}{N} \sum_i rr_i} * 100$$

2

3

4 where  $mw_i$  is the PNPR (v1 or v2) rainfall rate and  $rr_i$  is the TRMM-PR rainfall rate. N represents  
5 the number of pixels in each precipitation rate bin.

6 Considering the  $RB\%$  (top panel of Fig. 8) it is evident the better performance of PNPR v2 in the  
7 rain rate estimation over ocean (solid blue line) with respect to the PNPR v1 (dashed blue line). The  
8 high relative bias over ocean for low rain rates in the PNPR v1 is significantly reduced in PNPR v2.

9 In the interval between 0 and 4 mm h<sup>-1</sup> the  $RB\%$  ranges from 300% to 100% for the PNPR v1 and  
10 from 50% to 1% for the PNPR v2. In the following interval (4 to 10 mm h<sup>-1</sup>) the values varies from  
11 -5% to -40% for both the algorithms with a slightly better performance of PNPR v2.

12 Over land both the algorithms present similar performances, with a slightly better result for PNPR  
13 v2 (solid black line) for low rain rates (0 - 3 mm h<sup>-1</sup>), and lower  $RB\%$  of PNPR v1 (dashed black  
14 line) for higher rain rate values (> 3 mm h<sup>-1</sup>).

15 In the bottom panel of Fig. 8 AFSE $\%$  shows high values (> 250%) over ocean (blue curves) for very  
16 low rain rates (< 0.5 mm h<sup>-1</sup>) in PNPR v1, while for PNPR v2 AFSE $\%$  is much lower (< 200%). For  
17 higher rain rates the two curves are similar, with slightly better performance of PNPR v2 for rain  
18 rates < 2 mm h<sup>-1</sup>, and better performance of PNPR v1 for rain rates between 2 mm h<sup>-1</sup> and 6 mm h<sup>-1</sup>.

19 Over land, PNPR v2 shows lower AFSE $\%$  compared to PNPR v1 for mid to high rainfall rates (> 2  
20 mm h<sup>-1</sup>), while for lower rain rates the two curves are similar, with slightly better results for PNPR  
21 v2 for very low rain rates (< 0.5 mm h<sup>-1</sup>), and for PNPR v1 for rain rates between 0.5 mm h<sup>-1</sup> and 2  
22 mm h<sup>-1</sup>. It should be noted that overall this comparison shows a general agreement in the capability  
23 to estimate the precipitation by the two algorithms (as expected since they are based on the same  
24 physical foundation) with better performance of the ATMS version of PNPR for low precipitation  
25 rates, in particular over ocean (both in terms of  $RB\%$  and AFSE $\%$ ). For higher precipitation rates  
26 both PNPR versions tend to underestimate the precipitation (negative  $RB\%$ ), with larger (negative)  
27 bias of PNPR v2 than PNPR v1 over land.

28 It is worth noting that the main improvement of PNPR v2 with respect to PNPR v1 is the reduction  
29 of the relative bias ( $RB\%$ ) for low precipitation rates (where  $RB\%$  was higher) especially over ocean.  
30 Moreover, considering the AFSE $\%$ , the error is prevalently lower in version 2 even if the effect of  
31 the bias reduction is not taken into account.

32

### 33 5. Summary and conclusion

34 This paper describes the design of a new algorithm, PNPR v2, for estimation of precipitation on the  
35 ground for the cross-track ATMS radiometer, and presents the results of a verification study where  
36 the instantaneous precipitation rate estimates available from TRMM and GPM spaceborne radars  
37 are used as reference.

38 PNPR v2 has been designed for retrieval of precipitation in the MSG full disk area. The algorithm,  
39 based on a neural network approach, represents an evolution of the previous version PNPR v1,  
40 designed for the AMSU/MHS radiometer, with some changes made to take advantage of the  
41 improvements of ATMS with respect to AMSU/MHS. Similarly to the previous algorithm it is  
42 based on a single neural network for all types of surface background, trained using a large database  
43 based on 94 cloud-resolving model simulations over the European and the African areas.

44 The verification study carried out through a comparison with co-located observations of ATMS  
45 with the NASA/JAXA TRMM-PR and GPM-KuPR spaceborne radars analyzed on a 0.5° × 0.5°  
46 regular grid showed a substantial agreement of PNPR v2 with the precipitation products available  
47 from the two radars. In the comparison with TRMM-PR, over the African area, the CC has values  
48 between 0.64 (arid land) and 0.71 (vegetated land), and RMSE varies between 0.80 mm h<sup>-1</sup> (arid



1 land) and  $1.37 \text{ mm h}^{-1}$  (coast). The Adjusted FSE%, as a function of PR precipitation rate, ranges  
2 from 250% to 130% over ocean and from 250% to 100% over land in the interval from 0.1 to  $1 \text{ mm}$   
3  $\text{h}^{-1}$ . It is less than 50% for rain rate greater than  $7 \text{ mm h}^{-1}$  (ocean and land). In the comparison with  
4 GPM-KuPR over the European area the indexes are quite comparable with those over the African  
5 area, with lower correlation (0.59 over vegetated land and 0.57 over ocean) and RMSE ( $0.82 \text{ mm h}^{-1}$   
6 over vegetated land and  $0.71 \text{ mm h}^{-1}$  over ocean). It is worth noting that the study based on GPM-  
7 KuPR will be further developed in the future using a larger coincidence dataset and a more  
8 consolidated version of DPR precipitation products.

9 For reference, it is useful to compare these results with those found by other authors carrying out  
10 validation studies using ground-based radar data. Tang et al. (2014) investigated the performance of  
11 PMW precipitation products from 12 passive microwave radiometers, including AMSU-B (NOAA  
12 15, 16, 17) and MHS (NOAA 18, 19 and MetOp-A) rainfall rate estimates based on Ferraro et al.  
13 (2005) over a 3 year period. They found values of CC around 0.55 (on an annual scale, at  $0.25^\circ \times$   
14  $0.25^\circ$  regular grid) over the continental United States (land). They also analyzed the adjusted root-  
15 mean-square errors normalized with the precipitation rate (corresponding to the Adjusted FSE%  
16 used in this study) as a function of ground radar precipitation rate, and have found values ranging  
17 from about 600% at  $0.25 \text{ mm h}^{-1}$  to about 75% in the interval 6-16  $\text{mm h}^{-1}$  for winter, and from  
18 about 1200% at  $0.25 \text{ mm h}^{-1}$  to about 50% above the  $10 \text{ mm h}^{-1}$  for summer. Kidd et al. (2016)  
19 have analyzed the performance of precipitation retrieval from the MHS of the NASA Goddard  
20 PROFiling (GPROF) algorithm version developed for cross-track PMW sensors. Using quality  
21 controlled ground-based radar data over the United States from 6 March 2014 through 5 March  
22 2015, and computing the statistical scores over a  $1^\circ \times 1^\circ$  grid, they have found  $\text{CC} < 0.50$  over the  
23 western U.S., and  $> 0.60$  over the eastern U.S. It is worth noting that a comparison of the measured  
24 performances of different algorithms is very difficult and may not be significant if the conditions in  
25 which the various studies are performed are different (e.g. for the type and the quality of the  
26 reference data, different climate regimes, different matching procedure, and spatial resolution used  
27 in the analysis). Therefore, what can emerge from such results is that PNPR v2 performance is at  
28 least comparable with those of the analyzed algorithms.

29 In the comparison of PNPR v2 and PNPR v1 retrievals, performed over the African area and based  
30 on two years period of coincident observations of ATMS and AMSU/MHS radiometers with  
31 TRMM-PR, an appreciably better performance of PNPR v2 has been evidenced by statistical  
32 indexes (e.g. CC equal to 0.71 for PNPR v2, vs. 0.68 for PNPR v1 over vegetated land, and equal to  
33 0.69 for PNPR v2 vs. 0.61 for PNPR v1 over ocean), and by a general improvement of the estimate  
34 of low precipitation, mostly over ocean. The resulting differences can likely be attributed to  
35 improvements in the design of the neural network and also to the best technical features of ATMS  
36 compared to AMSU/MHS.

37 Overall, the two versions of PNPR algorithm have shown a general consistency in the results, as  
38 expected considering that both are based on the same physical basis (the training databases are  
39 based on the same cloud-resolving model and to the same radiative transfer model). It is worth  
40 noting that the achievement of consistency between products derived from different sensors is very  
41 relevant in the current GPM mission era, with constellation satellites (equipped with cross-track or  
42 conical scanning microwave radiometers) contributing to global coverage and higher temporal  
43 sampling of precipitation. This aspect has become very important also within the EUMETSAT H-  
44 SAF program, and represents a guideline for the development of PMW precipitation products.  
45 PNPR v2 and PNPR v1 for ATMS and AMSU/MHS, as well as other products for conically  
46 scanning radiometers (e.g. CDRD for SSMIS – Casella et al., 2013, Sanò et al., 2013), and new  
47 products for the other constellation radiometers are developed within H-SAF in this direction, with  
48 foreseen improvements of derived MW/IR products used in operational hydrology and near real  
49 time precipitation monitoring applications.

50 The results, however, have revealed a slight tendency of PNPR v2 to underestimate moderate to  
51 high precipitation, mostly over land, and overestimate moderate to light precipitation over the



1 ocean, especially compared to GPM-KuPR product over the North Atlantic Ocean. Besides well-  
2 known issues affecting PMW precipitation retrieval, such as non-uniform beam-filling effects  
3 related to small-scale rainfall structures associated with local convection and difficulties in the  
4 retrieval of warm or shallow rain processes, in addition to the lack of low frequency channels very  
5 useful for precipitation retrieval over ocean, other issues might be related to the use of spaceborne  
6 radar products as reference. The impact of sample volume discrepancies between radiometers and  
7 spaceborne radars, and uncertainties in the spaceborne radar estimates (due to attenuation  
8 correction, sensitivity thresholds, non-uniform beam filling effect), needs to be evaluated when  
9 using spaceborne radar precipitation estimates as reference. P NPR v2 will undergo thorough  
10 extensive validation within the EUMETSAT H-SAF program carried out by the H-SAF  
11 Precipitation Products Validation Service (Puca et al., 2014), using ground-based radars and rain  
12 gauges over Europe, and, in limited areas, over Africa, which will be useful to clarify some of these  
13 issues.

14 In spite of the above mentioned limitations, this study shows that the TRMM and GPM spaceborne  
15 radars can be very useful for an extensive verification, over long time periods, of consistency and  
16 accuracy of instantaneous precipitation rate estimates from different sensors. The use of spaceborne  
17 radars as reference overcomes some of the limitations in the use of ground-based data (such as  
18 inhomogeneity in their technical characteristics and data treatment, limited coverage, and beam  
19 blocking) providing consistent measurements around the globe, including remote areas where  
20 ground-based data are scarce or not available, and oceans.

21

22

### 23 Acknowledgments

24 The authors would like to thank the National Aeronautics and Space Administration (NASA,  
25 <http://www.nasa.gov>) for providing the TRMM-PR and GPM-KuPR data, the National Oceanic and  
26 Atmospheric Administration (NOAA, <http://www.class.ngdc.noaa.gov>) for providing the ATMS  
27 radiometer data, and The European Centre for Medium-Range Weather Forecasts (ECMWF,  
28 <http://www.ecmwf.int>) for providing the model reanalysis. This research was supported by  
29 EUMETSAT through the "Satellite Application Facility on Support to Operational Hydrology and  
30 Water Management" (H-SAF), by the Earth2Observe FP7 EU funded project, by the Italian Civil  
31 Protection Department. This research has been carried out within the collaboration between H-SAF  
32 and GPM (no-cost proposal approved by the NASA PMM Research Program) on the development  
33 of precipitation retrieval algorithms and validation activity.

34

35

36

37

38

39

40

41

42

43

44

45

46

47

48

49

50

51





## 1 References

- 2 Aires, F., Aznay, O., Prigent, C., Paul, M., and Bernardo F.: Synergistic multi-wavelength remote  
3 sensing versus a posteriori combination of retrieved products: Application for the retrieval of  
4 atmospheric profiles using MetOp-A, *J. Geophys. Res.*, 117, D18304,  
5 doi:10.1029/2011JD017188, 2012.
- 6 Anders, U. and Korn, O.: Model selection in neural networks, *Neural Networks*, 12, 309-323, 1999.
- 7 Bellerby, T., Todd, M., Kniveton, D., and Kidd, C.: Rainfall Estimation from a Combination of  
8 TRMM Precipitation Radar and GOES Multispectral Satellite Imagery through the Use of an  
9 Artificial Neural Network, *J. Appl. Meteorol.*, Volume 39, Issue 12, pp. 2115-2128, doi:  
10 [http://dx.doi.org/10.1175/1520-0450\(2001\)040<2115:REFACO>2.0.CO;2](http://dx.doi.org/10.1175/1520-0450(2001)040<2115:REFACO>2.0.CO;2), 2000.
- 11 Bellerby, T.J.: Satellite rainfall uncertainty estimation using an artificial neural network, *J.*  
12 *Hydrometeorol.*, 8, iss. 6, 1397-1412, doi: <http://dx.doi.org/10.1175/2007JHM846.1>, 2007.
- 13 Bennartz, R.: Optimal Convolution of AMSU-B to AMSU-A, *J. Atmos. Ocean. Tech.*, vol. 17,  
14 Issue 9, pp. 1215-1225, doi: [http://dx.doi.org/10.1175/1520-](http://dx.doi.org/10.1175/1520-0426(2000)017<1215:OCOABT>2.0.CO;2)  
15 [0426\(2000\)017<1215:OCOABT>2.0.CO;2](http://dx.doi.org/10.1175/1520-0426(2000)017<1215:OCOABT>2.0.CO;2), 2000.
- 16 Bennartz, R. and Petty, G.W.: The sensitivity of microwave remote sensing observations of  
17 precipitation to ice particle size distributions. *J. Appl. Meteorol.*, vol. 40, n. 3, pp. 345-364, doi:  
18 [http://dx.doi.org/10.1175/1520-0450\(2001\)040<0345:TSOMRS>2.0.CO;2](http://dx.doi.org/10.1175/1520-0450(2001)040<0345:TSOMRS>2.0.CO;2), 2001.
- 19 Bennartz, R. and Bauer, P.: Sensitivity of microwave radiances at 85-183 GHz to precipitating ice  
20 particles, *Radio Sci.*, 38, 4, 8075, doi:10.1029/2002RS002626, 2003.
- 21 Blackwell, W.J. and Chen, F.W.: Neural network applications in high-resolution atmospheric  
22 remote sensing, *Lincoln Lab. J.*, vol. 15, n. 2, pp. 299-322, 2005.
- 23 Boukabara, S.-A., Garrett, K., Blackwell, B.: ATMS Description & Expected Performances, Post-  
24 EPS User Consultation Workshop, Darmstadt, Germany, September 29-30, 2011.
- 25 Boukabara, S.-A., Garrett, K., Grassotti, C., Iturbide-Sanchez, F., Chen, W., Jiang, Z., Clough,  
26 S.A., Zhan, X., Liang, P., Liu, Q., Islam, T., Zubko, V., and Mims, A.: A physical approach for a  
27 simultaneous retrieval of sounding, surface, hydrometeor, and cryospheric parameters from  
28 SNPP/ATMS, *J. Geophys. Res. Atmos.*, vol. 118, pp. 12,600–12,619,  
29 doi:10.1002/2013JD020448, 2013.
- 30 Burns, B.A., Wu, X., and Diak, G.R.: Effects of precipitation and cloud ice on brightness  
31 temperatures in AMSU moisture channels, *IEEE T. Geosci. Remote*, vol. 35, n. 6, pp. 1429–  
32 1437, doi: 10.1109/36.649797, 1997.
- 33 Casella, D., Panegrossi, G., Sanò, P., Mugnai, A., Smith, E. A., Tripoli, G. J., Dietrich, S.,  
34 Formenton, M., Leung, W.Y., and Mehta, A.: Transitioning from CRD to CDRD in bayesian  
35 retrieval of rainfall from satellite passive microwave measurements: Part 2. Overcoming database  
36 profile selection ambiguity by consideration of meteorological control on microphysics, *IEEE T.*  
37 *Geosci. Remote*, 51, 4650-4671, 2013.
- 38 Casella, D., Panegrossi, G., Sanò, P., Milani, L., Petracca, M., and Dietrich, S.: A novel algorithm  
39 for detection of precipitation in tropical regions using PMW radiometers, *Atmos. Meas. Tech.*, 8,  
40 1217–1232, doi:10.5194/amt-8-1217-2015, 2015.
- 41 Chandrasekar, V., Le, M., and Awaka, J.: Vertical profile classification algorithm for GPM, *Int.*  
42 *Geosci. Remote Se.*, IGARSS 2014, pp. 3458 - 3761, doi: 10.1109/IGARSS.2014.6947301, 2014
- 43 Chen, F.W. and Staelin, D.H.: AIRS/AMSU/HSB precipitation estimates, *IEEE T. Geosci. Remote*,  
44 vol. 41, n. 2, pp. 410 – 417, doi: 10.1109/TGRS.2002.808322, 2003.
- 45 Chen, Y., Aires, F., Francis, J. A., and Miller, J. R.: Observed relationships between arctic longwave  
46 cloud forcing and cloud parameters using a neural network, *J. Climate*, 4087-4104, 2006.
- 47 Chen, F.W.; Bickmeier, L.J.; Blackwell, W.J.; Jairam, L.G.; and Leslie, V.R.:  
48 Neural network retrieval of precipitation using NPOESS microwave sensors, *Int. Geosci. Remote*  
49 *Se.*, IGARSS 2007, pp. 2272 - 2275, doi: 10.1109/IGARSS.2007.4423294, 2007.



- 1 Coulibaly P., Dibike Y.B., Anctil F.: Downscaling Precipitation and Temperature with Temporal  
2 Neural Networks. *J. Hydrometeorol.*, Volume 6, Issue 4, pp. 483-496,  
3 doi: <http://dx.doi.org/10.1175/JHM409.1>, 2005.
- 4 Draper, D.; Newell, D.; Wentz, F.; Krimchansky, S.; Skofronick-Jackson, G.: The Global  
5 Precipitation Measurement (GPM) Microwave Imager (GMI): Instrument Overview and Early  
6 On-Orbit Performance, *IEEE J. Sel. Top. Appl.*, vol. PP, n. 99, pp. 1 - 11, doi:  
7 10.1109/JSTARS.2015.2403303, 2015.
- 8 Ferraro, R.R. and Marks, G.F.: The development of SSM/I rain-rate retrieval algorithms using  
9 ground-based radar measurements, *J. Atmos. Ocean. Tech.*, vol. 12, n. 4, pp. 755-770,  
10 doi: [http://dx.doi.org/10.1175/1520-0426\(1995\)012<0755:TOSRR>2.0.CO;2](http://dx.doi.org/10.1175/1520-0426(1995)012<0755:TOSRR>2.0.CO;2), 1995.
- 11 Ferraro, R.R.: The Status of the NOAA/NESDIS Operational AMSU Precipitation Algorithm, 2nd  
12 Workshop of the International Precipitation Working Group, Monterey, 9 pp., 2004.
- 13 Ferraro, R. R., Weng, F., Grody, N. C., Zhao, L., Meng, H., Kongoli, C., Pellegrino, P., Qiu, S., and  
14 Dean, C.: NOAA operational hydrological products derived from the advanced microwave  
15 sounding unit, *IEEE T. Geosci. Remote*, 43 , 5, 1036-1049, 2005.
- 16 Funatsu, B.M., Claud, C., and Chaboureaud, J.-P.: Potential of Advanced Microwave Sounding Unit  
17 to identify precipitating systems and associated upper-level features in the Mediterranean region:  
18 Case studies, *J. Geophys. Res.*, 112, D17113, 19 pp., doi:10.1029/2006JD008297, 2007.
- 19 Funatsu, B.M., Claud, C., and Chaboureaud, J.-P.: Comparison between the large-scale environments  
20 of moderate and intense precipitating systems in the Mediterranean region, *Mon. Weather Rev.*,  
21 137, 11, 3933-3959, doi: <http://dx.doi.org/10.1175/2009MWR2922.1>, 2009.
- 22 Goldberg Mitchell D., Heather Kilcoyne, Harry Cikanek, and Ajay Mehta: Joint Polar Satellite  
23 System: The United States next generation civilian polar-orbiting environmental satellite system,  
24 *J. Geophys. Res. Atmos.*, vol. 118, pp. 13463–13475, doi:10.1002/2013JD020389, 2013.
- 25 Grody, N. C.: Classification of snow cover and precipitation using the special sensor microwave  
26 imager. *J. Geophys. Res.*, 96(D4), 7423–7435, doi:10.1029/91JD00045. 1991.
- 27 Hall, T., Brooks, H. E., and Doswell III, C. A.: Precipitation forecasting using a neural network,  
28 *Weather Forecast.*, vol. 14, n. 3, pp. 338-345 doi: [http://dx.doi.org/10.1175/1520-0434\(1999\)014<0338:PFUANN>2.0.CO;2](http://dx.doi.org/10.1175/1520-0434(1999)014<0338:PFUANN>2.0.CO;2), 1999.
- 30 Haupt, S.E., Pasini, A., Marzban, C.: *Artificial Intelligence Methods in the Environmental Sciences*,  
31 Springer, ISBN 978-1-4020-9117-9 (HB), 2009.
- 32 Heymsfield, G.M., Geerts, B., and Tian, L.: TRMM Precipitation Radar Reflectivity Profiles as  
33 Compared with High-Resolution Airborne and Ground-Based Radar Measurements, *J. Appl.*  
34 *Meteorol.*, vol. 39, n. 12, pp. 2080-2102, doi: [http://dx.doi.org/10.1175/1520-0450\(2001\)040<2080:TPRRPA>2.0.CO;2](http://dx.doi.org/10.1175/1520-0450(2001)040<2080:TPRRPA>2.0.CO;2), 2000.
- 36 Hirose, M., Shimizu, S., Oki, R., Iguchi, T., Short, D.A., and Nakamura K.: Incidence-Angle  
37 Dependency of TRMM PR Rain Estimates, *J. Atmos. Ocean. Tech.*, vol. 29, n. 2, pp. 192-206,  
38 doi: <http://dx.doi.org/10.1175/JTECH-D-11-00067.1>, 2012.
- 39 Hong, Y., Hsu, K.-L., Sorooshian, S., and Gao, X.: Precipitation estimation from remotely sensed  
40 imagery using an artificial neural network cloud classification system, *J. Appl. Meteorol.*, 43,  
41 1834-1853, 2004.
- 42 Hong, G., Heygster, G., Miao, J., and Kunzl, K.: Detection of tropical deep convective clouds from  
43 AMSU-B water vapor channels measurements, *J. Geophys. Res.*, 110, D05205,  
44 doi:10.1029/2004JD004949, 2005.
- 45 Hong, G., Heygster, G., Notholt, J., and Buehler, S.A.: Interannual to Diurnal Variations in Tropical  
46 and Subtropical Deep Convective Clouds and Convective Overshooting from Seven Years of  
47 AMSU-B Measurements, *J. Climate*, vol. 21, n. 17, pp. 4168-4189, doi:  
48 10.1175/2008JCLI1911.1, 2008.
- 49 Hou, A. Y., Kakar, R. K., Neeck, S., Azarbarzin, A. A., Kummerow, C. D., Kojima, M., Oki, R.,  
50 Nakamura, K., and Iguchi, T.: The global precipitation measurement mission, *B. Am. Meteorol.*  
51 *Soc.*, 95, 701-722, doi:10.1175/BAMS-D-13-00164.1, 2014.



- 1 Hsu, K.-L., Gao, X., Sorooshian, S., and Gupta, H.V.: Precipitation estimation from remotely  
2 sensed information using artificial neural networks, *J. Appl. Meteorol.*, vol. 36, n. 9, pp. 1176-  
3 1190, doi: [http://dx.doi.org/10.1175/1520-0450\(1997\)036<1176:PEFRSI>2.0.CO;2](http://dx.doi.org/10.1175/1520-0450(1997)036<1176:PEFRSI>2.0.CO;2), 1997.
- 4 Huffman, G.J., Bolvin, D.T., Nelkin, E.J., Wolff, D.B., Adler, R.F., Gu, G., Hong, Y., Bowman,  
5 K.P., Stocker, E.F.: The TRMM Multisatellite Precipitation Analysis (TMPA): Quasi-Global,  
6 Multiyear, Combined-Sensor Precipitation Estimates at Fine Scales, *J. Hydrometeorol.*, vol. 8, n.  
7 1, pp. 38-55, doi: <http://dx.doi.org/10.1175/JHM560.1>, 2007.
- 8 Huffman, G.J., Bolvin, D.T., Braithwaite, D., Hsu, K., Joyce, R., Kidd, C., Nelkin, E.J., and  
9 Pingping, X.: NASA Global Precipitation Measurement (GPM) Integrated Multi-satellitE  
10 Retrievals for GPM (IMERG), ATBD v. 4.5, NASA, pp. 66, available at:  
11 [http://pmm.nasa.gov/sites/default/files/document\\_files/IMERG\\_ATBD\\_V4.5.pdf](http://pmm.nasa.gov/sites/default/files/document_files/IMERG_ATBD_V4.5.pdf), 2015
- 12 Iguchi, T., Kozu, T., Meneghini, R., Awaka, J., and Okamoto, K.: Rain-Profiling Algorithm for the  
13 TRMM Precipitation Radar, *J. Appl. Meteorol.*, vol. 39, n.12, pp. 2038-2052,  
14 doi: [http://dx.doi.org/10.1175/1520-0450\(2001\)040<2038:RPAFTT>2.0.CO;2](http://dx.doi.org/10.1175/1520-0450(2001)040<2038:RPAFTT>2.0.CO;2), 2000.
- 15 Iguchi, T., Kozu, T., Kwiatkowski, J., Meneghini, R., Awaka, J., and Okamoto, K.: Uncertainties  
16 in the Rain Profiling Algorithm for the TRMM Precipitation Radar, *J. Meteorol. Soc. Jpn.*, vol.  
17 87A, 1-30, doi:10.2151/jmsj.87A.1, 2009.
- 18 Iturbide-Sanchez, F., Boukabara, S.-A., Ruiyue Chen, Garrett, K., Grassotti, C., Wanchun Chen,  
19 Fuzhong Weng: Assessment of a Variational Inversion System for Rainfall Rate Over Land and  
20 Water Surfaces, *IEEE T. Geosci. Remote*, vol. 49, n. 9, pp. 3311-3333, doi:  
21 [10.1109/TGRS.2011.2119375](http://dx.doi.org/10.1109/TGRS.2011.2119375), 2011.
- 22 Kidd, C.: On rainfall retrieval using polarization-corrected temperatures, *Int. J. Remote Sens.*, vol.  
23 19, n. 5, pp. 981-996, doi: [10.1080/014311698215829](http://dx.doi.org/10.1080/014311698215829), 1998.
- 24 Kidd, C., Matsui, T., Chern, J., Mohr, K., Kummerow, C., and Randel, D.: Global Precipitation  
25 Estimates from Cross-Track Passive Microwave Observations Using a Physically Based Retrieval  
26 Scheme, *J. Hydrometeorol.*, vol. 17, n. 1, pp. 383-400, doi: <http://dx.doi.org/10.1175/JHM-D-15-0051.1>, 2016.
- 28 Kirstetter, P. E., Hong, Y., Gourley, J. J., Chen, S., Flamig, Z., Zhang, J., Schwaller, M.,  
29 Petersen, W., Amitai, E.: Toward a Framework for Systematic Error Modeling of Spaceborne  
30 Precipitation Radar with NOAA/NSSL Ground Radar-Based National Mosaic QPE, *J.*  
31 *Hydrometeorol.*, vol. 13, n. 4, pp. 1285-1300, doi: <http://dx.doi.org/10.1175/JHM-D-11-0139.1>,  
32 2012.
- 33 Kirstetter, P-E., Viltard, N., and Gosset, M.: An error model for instantaneous satellite rainfall  
34 estimates: evaluation of BRAIN-TMI over West Africa, *Q. J. R. Meteorol. Soc.*, vol. 139, pp.  
35 894-911, doi:10.1002/qj.1964, 2013.
- 36 Kongoli, C., Meng, H., Dong, J., and Ferraro, R.: A snowfall detection algorithm over land utilizing  
37 high-frequency passive microwave measurements—Application to ATMS, *J. Geophys. Res.*  
38 *Atmos.*, vol. 120, n. 5, pp. 1918-1932, doi:10.1002/2014JD022427, 2015.
- 39 Krasnopolsky, V. M., Fox-Rabinovitz, M. S., and Belochitski, A. A.: Decadal climate simulations  
40 using accurate and fast neural network emulation of full, longwave and shortwave, radiation,  
41 *Mon. Weather Rev.*, 3683-3695, doi: [10.1175/2008MWR2385.1](http://dx.doi.org/10.1175/2008MWR2385.1), 2008.
- 42 Kummerow, C.D., Ringerud, S., Crook, J., Randel D., and Berg, W.: An Observationally  
43 Generated A Priori Database for Microwave Rainfall Retrievals, *J. Atmos. Ocean. Tech.*, vol. 28,  
44 n. 2, pp. 113-130, doi: [10.1175/2010JTECHA1468.1](http://dx.doi.org/10.1175/2010JTECHA1468.1), 2011.
- 45 Kummerow, C.D., Randel, D.L., Kulie, M., Wang, N.-Y., Ferraro, R., Munchak, S.J., Petkovic, V.:  
46 The Evolution of the Goddard Profiling Algorithm to a Fully Parametric Scheme, *J. Atmos.*  
47 *Ocean. Tech.*, vol. 32, n. 12, pp. 2265-2280, doi: <http://dx.doi.org/10.1175/JTECH-D-15-0039.1>,  
48 2015.
- 49 Laviola S. and Levizzani, V.: The 183-WLS fast rain rate retrieval algorithm. Part I: Retrieval  
50 design, *Atmos. Res.*, vol. 99, pp. 443-461, doi:10.1016/j.atmosres.2010.11.013, 2011.



- 1 Le, M., and Chandrasekar, V.: Hydrometeor Profile Characterization Method for Dual-Frequency  
2 Precipitation Radar Onboard the GPM, *IEEE T. Geosci. Remote*, vol. 51, n. 6, pp. 3648 -  
3 3658, doi: 10.1109/TGRS.2012.2224352, 2013a.
- 4 Le, M., and Chandrasekar, V.: Precipitation Type Classification Method for Dual-Frequency  
5 Precipitation Radar (DPR) Onboard the GPM, *IEEE T. Geosci. Remote*, vol. 51, n. 3, pp. 1784 -  
6 1790, doi: 10.1109/TGRS.2012.2205698, 2013b.
- 7 Leslie, R. V., Blackwell, W. J., Bickmeier, L. J., and Jaram, L. G.: Neural network microwave  
8 precipitation retrievals and modeling results, *Proc. SPIE*, 7154, 715406-8, doi:10.1117/12.804815,  
9 2008.
- 10 Liao, L., Meneghini, R., and Iguchi, T.: Comparisons of rain rate and reflectivity factor derived  
11 from the TRMM Precipitation Radar and the WSR-88D over the Melbourne, Florida site, *J.*  
12 *Atmos. Ocean. Tech.*, vol. 18, n. 12, pp. 1959–1974, doi: [http://dx.doi.org/10.1175/1520-](http://dx.doi.org/10.1175/1520-0426(2001)018<1959:CORRAR>2.0.CO;2)  
13 [0426\(2001\)018<1959:CORRAR>2.0.CO;2](http://dx.doi.org/10.1175/1520-0426(2001)018<1959:CORRAR>2.0.CO;2), 2001.
- 14 Liao, L., Meneghini, R., Tokay, A.: Uncertainties of GPM DPR Rain Estimates Caused by DSD  
15 Parameterizations, *J. Appl. Meteorol. Clim.*, vol. 53, n. 11, pp. 2524-2537,  
16 doi: <http://dx.doi.org/10.1175/JAMC-D-14-0003.1>, 2014.
- 17 Lin X. and Hou, A. Y.: Evaluation of coincident passive microwave estimates using TRMM PR and  
18 ground measurements as references, *J. Appl. Meteorol. Clim.*, vol. 47, n. 12, pp. 3170-3187, doi:  
19 [10.1175/2008JAMC1893.1](http://dx.doi.org/10.1175/2008JAMC1893.1), 2008.
- 20 Liou, Y.-A., Tzeng, Y.C., and Chen, K.S.: A neural-network approach to radiometric sensing of  
21 land-surface parameters, *IEEE T. Geosci. Remote*, vol. 37, n. 6, pp. 2718-2724,  
22 doi: 10.1109/36.803419, 1999.
- 23 Mahesh, C., Satya Prakash, Sathiyamoorthy, V., and Gairola, R.M.: Artificial neural network based  
24 microwave precipitation estimation using scattering index and polarization corrected temperature,  
25 *Atmos. Res.*, vol. 102, n. 3, pp. 358-364, doi: 10.1016/j.atmosres.2011.09.003, 2011.
- 26 Marzban, C.: Neural Networks for Postprocessing Model Output: ARPS, *Mon. Weather Rev.*, vol.  
27 131, pp. 1103-1111, doi: [http://dx.doi.org/10.1175/1520-](http://dx.doi.org/10.1175/1520-0493(2003)131<1103:NNFPMO>2.0.CO;2)  
28 [0493\(2003\)131<1103:NNFPMO>2.0.CO;2](http://dx.doi.org/10.1175/1520-0493(2003)131<1103:NNFPMO>2.0.CO;2), 2003.
- 29 Marzban C.: Basic statistics and basic AI: neural networks, in: *Artificial Intelligence Methods in the*  
30 *Environmental Science*, edited by: Haupt, S.E., Pasini, A., and Marzban C., Springer, 15-47,  
31 2009.
- 32 Mugnai, A., Smith, E. A., and Tripoli, G. J.: Foundations for statistical physical precipitation  
33 retrieval from passive microwave satellite measurement. Part II : Emission-source and generalized  
34 weighting-function properties of a time-dependent cloud-radiation model, *J. Appl. Meteorol.*, 32,  
35 17-39, 1993.
- 36 Mugnai, A., Casella, D., Cattani, E., Dietrich, S., Laviola, S., Levizzani, V., Panegrossi, G.,  
37 Petracca, M., Sanò, P., Di Paola, F., Biron, D., De Leonibus, L., Melfi, D., Rosci, P., Vocino, A.,  
38 Zauli, F., Puca, S., Rinollo, A., Milani, L., Porcù, F., and Gattari, F.: Precipitation products from  
39 the hydrology SAF, *Nat. Hazards Earth Syst. Sci.*, vol. 13, n. 8, pp. 1959-1981,  
40 doi:10.5194/nhess-13-1959-2013, 2013a.
- 41 Mugnai, A., Smith, E. A., Tripoli, G. J., Bizzarri, B., Casella, D., Dietrich, S., Di Paola, F.,  
42 Panegrossi, G., and Sanò, P.: CDRD and PNPR satellite passive microwave precipitation retrieval  
43 algorithms: euroTRMM/EURAINSAT Origins and H-SAF operations, *Nat. Hazards Earth Syst.*  
44 *Sci.*, vol. 13, pp. 887–912, doi:10.5194/nhess-13-887-2013, 2013b.
- 45 Newell, D., Draper, D., Figgins, D., Berdanier, B., Kubitschek, M., Holshouser, D., Sexton,  
46 A., Krimchansky, S., Wentz, F., and Meissner, T.: GPM microwave imager key performance and  
47 calibration results, *Int. Geosci. Remote Se.*, *IGARSS 2014*, pp. 3754 -  
48 3757, doi: 10.1109/IGARSS.2014.6947300, 2014.
- 49 Panegrossi, G., Dietrich, S., Marzano, F. S., Mugnai, A., Smith, E. A., Xiang, X., Tripoli, G. J.,  
50 Wang, P. K., and Póiares Baptista, J. V. P.: Use of cloud model microphysics for passive



- 1 microwave-based precipitation retrieval: significance of consistency between model and  
2 measurement manifolds, *J. Atmos. Sci.*, vol. 55, pp. 1644-1673, 1998.
- 3 Panegrossi, G., Casella, D., Dietrich, S., Marra, A. C., Milani, L., Petracca, M., Sanò, P., and  
4 Mugnai, A.: CDRD and PNPR passive microwave precipitation retrieval algorithms: extension to  
5 the MSG full disk area, Proc. 2014 EUMETSAT Meteorological Satellite Conference, Geneva,  
6 [https://www.eumetsat.int/website/home/News/ConferencesandEvents/DAT\\_2076129.html](https://www.eumetsat.int/website/home/News/ConferencesandEvents/DAT_2076129.html), 2014.
- 7 Panegrossi, G., Casella, D., Dietrich, S., Marra, A.C., Petracca, M., Sanò, P., Baldini, L., Roberto,  
8 N., Adirosi, E., Cremonini, R., Bechini, R., Vulpiani, G.: Use of the constellation of PMW  
9 radiometers in the GPM ERA for heavy precipitation event monitoring and analysis during fall  
10 2014 in Italy, *Int. Geosci. Remote Se., IGARSS 2015*, pp. 5150-5153, doi:  
11 10.1109/IGARSS.2015.7326993, 2015.
- 12 Panegrossi, G., Casella, D., Dietrich, S., Marra, A.C., Sanò, P., Mugnai, A., Baldini, L., Roberto,  
13 N., Adirosi, E., Cremonini, R., Bechini, R., Vulpiani, G., Petracca, M., and Porcù, F.: Use of the  
14 GPM Constellation for Monitoring Heavy Precipitation Events Over the Mediterranean Region,  
15 *IEEE J. Sel. Top. Appl.*, vol. PP, n. 99, pp. 1-21, doi: 10.1109/JSTARS.2016.2520660, 2016.
- 16 Petković, V., and Kummerow C.D.: Performance of the GPM Passive Microwave Retrieval in the  
17 Balkan Flood Event of 2014, *J. Hydrometeorol.*, vol. 16, n. 6,  
18 doi: <http://dx.doi.org/10.1175/JHM-D-15-0018.1>, 2015.
- 19 Qiu, S., Pellegrino, P., Ferraro, R., and Zhao, L.: The improved AMSU rain-rate algorithm and its  
20 evaluation for a cool season event in the Western United States, *Weather Forecast.*, vol. 20, n.5,  
21 pp. 761-774, doi: <http://dx.doi.org/10.1175/WAF880.1>, 2005.
- 22 Sanò, P., Casella, D., Mugnai, A., Schiavon, G., Smith, E. A., and Tripoli, G. J.: Transitioning from  
23 CRD to CDRD in bayesian retrieval of rainfall from satellite passive microwave measurements:  
24 Part 1. Algorithm description and testing, *IEEE T. Geosci. Remote*, 51, 4119-4143, doi:  
25 10.1109/TGRS.2012.2227332, 2013.
- 26 Sanò, P., Panegrossi, G., Casella, D., Di Paola, F., Milani, L., Mugnai, A., Petracca, M., and  
27 Dietrich, S.: The Passive microwave Neural network Precipitation Retrieval (PNPR) algorithm for  
28 AMSU/MHS observations: description and application to European case studies, *Atmos. Meas.*  
29 *Tech.*, vol. 8, pp. 837–857, doi:10.5194/amt-8-837-2015, 2015.
- 30 Sarma, D.K., Konwar, M., Sharma, S., Pal, S., Das, J., De, U.K., Viswanathan, G.: An Artificial-  
31 Neural-Network-Based Integrated Regional Model for Rain Retrieval Over Land and Ocean,  
32 *IEEE T. Geosci. Remote*, vol. 46, n. 6, pp. 1689 - 1696, doi: 10.1109/TGRS.2008.916469, 2008.
- 33 Shank, D.B., Hoogenboom, G., McClendon, R.W.: Dewpoint Temperature Prediction Using  
34 Artificial Neural Networks. *J. Appl. Meteorol. Clim.*, vol. 47, n. 6, pp. 1757-1769,  
35 doi: <http://dx.doi.org/10.1175/2007JAMC1693.1>, 2008.
- 36 Shimozuma, T., and Seto, S.: Evaluation of KUPR algorithm in matchup cases of GPM and  
37 TRMM, *Int. Geosci. Remote Se., IGARSS 2015*, pp. 5134 -  
38 5137, doi: 10.1109/IGARSS.2015.7326989, Milan 2015.
- 39 Schumacher, C. and Houze Jr., R.A.: Stratiform Rain in the Tropics as Seen by the TRMM  
40 Precipitation Radar, *J. Climate*, vol. 16, n.11, pp. 1739-1756, doi: [http://dx.doi.org/10.1175/1520-0442\(2003\)016<1739:SRITTA>2.0.CO;2](http://dx.doi.org/10.1175/1520-0442(2003)016<1739:SRITTA>2.0.CO;2), 2003.
- 42 Shi, L.: Retrieval of Atmospheric Temperature Profiles from AMSU-A Measurement Using a  
43 Neural Network Approach, *J. Atmos. Ocean. Tech.*, vol. 18, n. 3, pp. 340-347,  
44 doi: [http://dx.doi.org/10.1175/1520-0426\(2001\)018<0340:ROATPF>2.0.CO;2](http://dx.doi.org/10.1175/1520-0426(2001)018<0340:ROATPF>2.0.CO;2), 2001.
- 45 Smith, E. A., Leung, H. W.-Y., Elsner, J. B., Mehta, A. V., Tripoli, G. J., Casella, D., Dietrich, S.,  
46 Mugnai, A., Panegrossi, G., and Sanò, P.: Transitioning from CRD to CDRD in bayesian retrieval  
47 of rainfall from satellite passive microwave measurements: Part 3. Identification of optimal  
48 meteorological tags, *Nat. Hazards Earth Syst. Sci*, 13, 1185–1208, doi:10.5194/nhess-13-1185-  
49 2013, 2013.
- 50 Sorooshian, S., Hsu, K. -L., Gao, X., Gupta, H. V., Imam, B., and Braithwaite, D.: Evaluation of  
51 PERSIANN system satellite-based estimates of tropical rainfall, *B. Am. Meteorol. Soc.*, vol. 81,



- 1 n. 9, pp. 2035-2046, doi: [http://dx.doi.org/10.1175/1520-0477\(2000\)081<2035:EOPSSSE>2.3.CO;2](http://dx.doi.org/10.1175/1520-0477(2000)081<2035:EOPSSSE>2.3.CO;2), 2000.
- 2
- 3 Staelin, D. H., Chen, F.W., and Fuentes, A.: Precipitation measurements using 183-GHz AMSU  
 4 satellite observations, *Int. Geosci. Remote Se., IGARSS 1999 Proceedings*, vol. 4, pp. 2069-  
 5 2071, doi: 10.1109/IGARSS.1999.775034, 1999.
- 6 Staelin, D. H. and Chen, F. W.: Precipitation observations near 54 and 183 GHz using the NOAA-  
 7 15 satellite, *IEEE T. Geosci. Remote*, 38, 2322-2332, 2000.
- 8 Surussavadee, C. and Staelin, D. H.: Millimeter-wave precipitation retrievals and observed-vs.-  
 9 simulated radiance distributions: sensitivity to assumptions, *J. Atmos. Sci.*, 64, 3808-3826, 2007.
- 10 Surussavadee, C. and Staelin, D. H.: Global millimeter-wave precipitation retrievals trained with a  
 11 cloud-resolving numerical weather prediction model, Part I: Retrieval design, *IEEE T. Geosci.*  
 12 *Remote*, 46, 99-108, doi:10.1109/TGRS.2007.908302, 2008a.
- 13 Surussavadee, C. and Staelin, D. H.: Global millimeter-wave precipitation retrievals trained with a  
 14 cloud-resolving numerical weather prediction model, Part II: Performance evaluation, *IEEE T.*  
 15 *Geosci. Remote*, 46, 109-118, doi:10.1109/TGRS.2007.908299, 2008b.
- 16 Surussavadee, C. and Staelin, D. H.: Satellite Retrievals of Arctic and Equatorial Rain and Snowfall  
 17 Rates Using Millimeter Wavelengths, *IEEE T. Geosci. Remote*, vol. 47, n.11, pp. 3697-3707,  
 18 2009.
- 19 Surussavadee, C. and Staelin, D.H.: Global precipitation retrieval algorithm trained for SSMIS  
 20 using a Numerical Weather Prediction Model: Design and evaluation, *Int. Geosci. Remote Se.,*  
 21 *IGARSS 2010*, pp. 2341 - 2344, doi: 10.1109/IGARSS.2010.5649699, 2010.
- 22 Surussavadee, C., Blackwell, W.J., Entekhabi, D. and Leslie, R.V.: A global precipitation retrieval  
 23 algorithm for SUOMI NPP ATMS, *Int. Geosci. Remote Se., IGARSS 2012*, pp. 1924 – 1927, doi:  
 24 10.1109/IGARSS.2012.6351128, Munich, 2012.
- 25 Tang, L., Tian, Y., and Lin, X.: Validation of precipitation retrievals over land from satellite-based  
 26 passive microwave sensors, *J. Geophys. Res. Atmos.*, vol. 119, pp. 4546–4567,  
 27 doi:10.1002/2013JD020933, 2014.
- 28 Tapiador, F.J., Kidd, C., Levizzani, V., and Marzano, F.S.: A Neural Networks–Based Fusion  
 29 Technique to Estimate Half-Hourly Rainfall Estimates at 0.1° Resolution from Satellite Passive  
 30 Microwave and Infrared Data, *J. Appl. Meteorol.*, vol. 43, n. 4, pp. 576-594, doi:  
 31 [http://dx.doi.org/10.1175/1520-0450\(2004\)043<0576:ANNFTT>2.0.CO;2](http://dx.doi.org/10.1175/1520-0450(2004)043<0576:ANNFTT>2.0.CO;2), 2004.
- 32 Tian, Y., Peters-Lidard, C.D., Eylander, J.B., Joyce, R.J., Huffman, G.J., Adler, R.F., Hsu, K.,  
 33 Turk, F.J., Garcia, M., and Zeng, J.: Component analysis of errors in satellite-based precipitation  
 34 estimates, *J. Geophys. Res.*, vol. 114, D24101, doi: 10.1029/2009JD011949, 2009.
- 35 Tian, Y., Nearing, G.S., Peters-Lidard, C.D., Harrison, K.W., Tang, L.: Performance Metrics, Error  
 36 Modeling, and Uncertainty Quantification, *Mon. Weather Rev.*, Vol. 144, n. 2, pp. 607-613,  
 37 doi: <http://dx.doi.org/10.1175/MWR-D-15-0087.1>, 2016.
- 38 Toyoshima, K., Masunaga, H., and Furuzawa, F.A.: Early Evaluation of Ku- and Ka-Band  
 39 Sensitivities for the Global Precipitation Measurement (GPM) Dual-Frequency Precipitation  
 40 Radar (DPR), *SOLA*, vol. 11, pp. 14–17, doi:10.2151/sola.2015-004, 2015.
- 41 Tripoli, G. J.: A nonhydrostatic mesoscale model designed to simulate scale interaction, *Mon.*  
 42 *Weather Rev.*, 120, 1342–1359, 1992.
- 43 Tripoli, G. J. and Smith, E. A. Introducing Variable-Step Topography (VST) coordinates within  
 44 dynamically constrained Nonhydrostatic Modeling Systems (NMW), part 1: VST formulation  
 45 within NMS host model framework, *Dynam. Atmos. Oceans*, vol. 66, pp. 28-57, doi:  
 46 10.1016/j.dynatmoe.2014.01.001, 2014a.
- 47 Tripoli, G. J. and Smith, E. A.: Introducing Variable-Step Topography (VST) coordinates within  
 48 dynamically constrained Nonhydrostatic Modeling Systems (NMW), part 2: VST performance on  
 49 orthodox obstacle flows, *Dynam. Atmos. Oceans*, vol. 66, pp. 10-27, doi:  
 50 10.1016/j.dynatmoe.2014.01.003, 2014b.



- 1 Wang, J. R., Wilheit, T. T., and Chang, L. A.: Retrieval of total precipitable water using radiometric  
2 measurements near 92 and 183 GHz, *J. Appl. Meteorol.*, vol. 28, n. 2, pp. 146-154,  
3 doi: [http://dx.doi.org/10.1175/1520-0450\(1989\)028<0146:ROTPWU>2.0.CO;2](http://dx.doi.org/10.1175/1520-0450(1989)028<0146:ROTPWU>2.0.CO;2), 1989.
- 4 Wang, J. R., Zhan, J., and Racette, P.: Storm-associated microwave radiometric signatures in the  
5 frequency range of 90–220 GHz, *J. Atmos. Ocean. Tech.*, vol. 14, n.1, pp. 13-31,  
6 doi: [http://dx.doi.org/10.1175/1520-0426\(1997\)014<0013:SAMRSI>2.0.CO;2](http://dx.doi.org/10.1175/1520-0426(1997)014<0013:SAMRSI>2.0.CO;2), 1997.
- 7 Weng, F., Zou, X., Wang, X., Yang, S., and Goldberg, M.D.: Introduction to Suomi national  
8 polar-orbiting partnership advanced technology microwave sounder for numerical weather  
9 prediction and tropical cyclone applications, *J. Geophys. Res.*, vol. 117, D19112,  
10 doi:10.1029/2012JD018144, 2012.
- 11 You, Y., and Liu, G.: The relationship between surface rainrate and water paths and its implications  
12 to satellite rainrate retrieval. *J. Geophys. Res.*, vol. 117, D13207, doi:10.1029/2012JD017662,  
13 2012.
- 14 You, Y., Wang, N.-Y., and Ferraro, R.: A prototype precipitation retrieval algorithm over land  
15 using passive microwave observations stratified by surface condition and precipitation vertical  
16 structure. *J. Geophys. Res. Atmos.*, vol. 120, n.11, pp. 5295–5315. doi: 10.1002/2014JD022534,  
17 2015.
- 18 Zou, X., Weng, F., Zhang, B., Lin, L., Qin, Z. and Tallapragada, V.: Impacts of assimilation of  
19 ATMS data in HWRP on track and intensity forecasts of 2012 four landfall hurricanes, *J.*  
20 *Geophys. Res. Atmos.*, vol. 118, n. 11, 558–11, 576, doi:10.1002/2013JD020405, 2013.

21  
22  
23  
24  
25  
26  
27  
28  
29  
30  
31  
32  
33  
34  
35  
36  
37  
38  
39  
40  
41  
42  
43  
44  
45  
46  
47  
48  
49  
50  
51



1 Table 1 - Results of the tests for the selection of the inputs to the NN. Input combinations are listed  
 2 in the first column ( $\Delta_F = \Delta_{13}, \Delta_{37}, \Delta_{17}$ ), R indicates the correlation coefficient, MSE the mean  
 3 squared error, CV the cross-validation index (subscripts L and CV indicate the learning and cross-  
 4 validation phases).  
 5

INPUT	$R_L$	$MSE_L$	$R_{CV}$	CV
$\Delta_F$	<b>0.85</b>	<b>0.39</b>	<b>0.76</b>	<b>0.42</b>
$\Delta_F$ and $\Delta_{14}, \Delta_{24}, \Delta_{27}$	0.78	0.64	0.70	0.68
$\Delta_F$ and $\Delta_{14}, \Delta_{24}$	0.89	0.37	0.80	0.42
$\Delta_F$ and $\Delta_{14}, \Delta_{27}$	0.83	0.49	0.78	0.53
$\Delta_F$ and $\Delta_{24}, \Delta_{27}$	0.81	0.50	0.70	0.54
$\Delta_F$ and $\Delta_{14}$	0.87	0.37	0.79	0.41
<b><math>\Delta_F</math> and <math>\Delta_{24}</math></b>	<b>0.92</b>	<b>0.32</b>	<b>0.87</b>	<b>0.35</b>
$\Delta_F$ and $\Delta_{27}$	0.83	0.48	0.68	0.52

6  
7  
8  
9  
10  
11  
12  
13  
14  
15  
16  
17  
18  
19  
20  
21  
22  
23  
24  
25





1 Table 2 - Contingency table of PNPR v2 retrievals relative to TRMM-PR measurements  
 2

		Radar rain rate (mm h <sup>-1</sup> )			
		0.01 ≤ Rad ≤ 0.25	0.25 < Rad ≤ 1.0	1.0 < Rad ≤ 5.0	5.0 < Rad ≤ 15.0
PNPR v2 rain rate (mm h <sup>-1</sup> )	Vegetated land				
	0.01 ≤ PNPR v2 ≤ 0.25	<b>80.3%</b>	35.4%	2.9%	0.0%
	0.25 < PNPR v2 ≤ 1.0	17.8%	<b>50.4%</b>	35.1%	6.2%
	1.0 < PNPR v2 ≤ 10.0	1.9%	13.6%	<b>54.6%</b>	38.4%
	5.0 < PNPR v2 ≤ 15.0	0.0%	0.6%	7.4%	<b>55.4%</b>
	Coast				
	0.01 ≤ PNPR v2 ≤ 0.25	<b>86.4%</b>	34.0%	7.1%	0.0%
	0.25 < PNPR v2 ≤ 1.0	12.1%	<b>52.3%</b>	31.1%	0.0%
	1.0 < PNPR v2 ≤ 10.0	1.5%	13.0%	<b>51.0%</b>	26.6%
	5.0 < PNPR v2 ≤ 15.0	0.0%	0.7%	10.8%	<b>73.4%</b>
	Ocean				
	0.01 ≤ PNPR v2 ≤ 0.25	<b>85.2%</b>	32.5%	3.7%	0.0%
	0.25 < PNPR v2 ≤ 1.0	13.1%	<b>51.4%</b>	30.8%	7.5%
	1.0 < PNPR v2 ≤ 10.0	1.7%	16.0%	<b>54.7%</b>	39.1%
	5.0 < PNPR v2 ≤ 15.0	0.0%	0.1%	10.8%	<b>53.4%</b>
	Arid land				
0.01 ≤ PNPR v2 ≤ 0.25	<b>72.1%</b>	27.6%	1.2%	n/a	
0.25 < PNPR v2 ≤ 1.0	27.6%	<b>53.4%</b>	37.1%	n/a	
1.0 < PNPR v2 ≤ 10.0	0.3%	18.7%	<b>58.0%</b>	n/a	
5.0 < PNPR v2 ≤ 15.0	0.0%	0.3%	3.7%	n/a	

3  
 4  
 5  
 6  
 7  
 8  
 9  
 10  
 11  
 12  
 13  
 14  
 15  
 16  
 17  
 18



1  
2  
3  
4  
5  
6  
7  
8  
9  
10  
11  
12  
13  
14  
15  
16  
17  
18  
19  
20  
21  
22  
23  
24  
25  
26  
27  
28  
29

Table 3 - Performace indexes for the different background surfaces

	Vegetated land	Ocean	Coast	Arid land
Perf. Index	69.0%	76.0%	75.7%	66.7%



1 Table 4 - Statistical indexes obtained in the comparisons of PNPR v2 retrievals with GPM-KuPR  
2 and TRMM-PR products

3

	Vegetated land GPM-KuPR /TRMM-PR	Ocean GPM-KuPR /TRMM-PR
BIAS (mm h <sup>-1</sup> )	0.15/-0.08	-0.04/0.05
CC	0.70/0.71	0.70/0.69
RMSE (mm h <sup>-1</sup> )	1.08/1.11	1.21/1.30

4

5

6

7

8

9

10

11

12

13

14

15

16

17

18

19

20

21

22

23

24

25

26



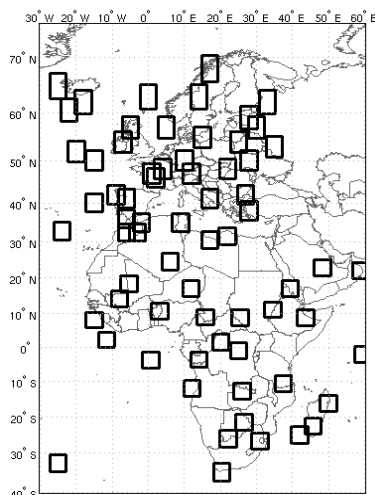
1 Table 5– Statistical indexes of the comparison of PNPR v1 and PNPR v2 vs TRMM-PR retrievals

2  
3  
4  
5  
6  
7  
8  
9  
10  
11  
12  
13  
14  
15  
16  
17  
18  
19  
20  
21  
22  
23  
24  
25  
26  
27  
28  
29  
30  
31  
32  
33  
34  
35  
36  
37  
38  
39  
40  
41  
42  
43  
44  
45

	Arid land PNPR v1/PNPR v2	Vegetated land PNPR v1/PNPR v2	Coast PNPR v1/PNPR v2	Ocean PNPR v1/PNPR v2
BIAS (mm h <sup>-1</sup> )	0.30/-0.05	-0.09/-0.08	0.15/0.05	0.63/0.05
CC	0.66/0.64	0.68/0.71	0.75/0.65	0.60/0.69
RMSE (mm h <sup>-1</sup> )	1.84/0.80	1.66/1.11	1.73/1.37	2.25/1.30

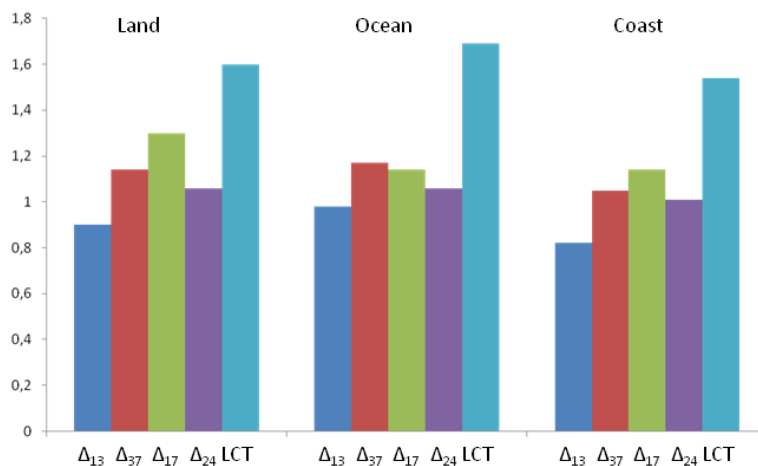


1  
 2



3  
 4  
 5  
 6  
 7  
 8  
 9  
 10  
 11  
 12

Figure 1 – Geographical location of the inner domain of the 94 NMS simulations over European and African areas.

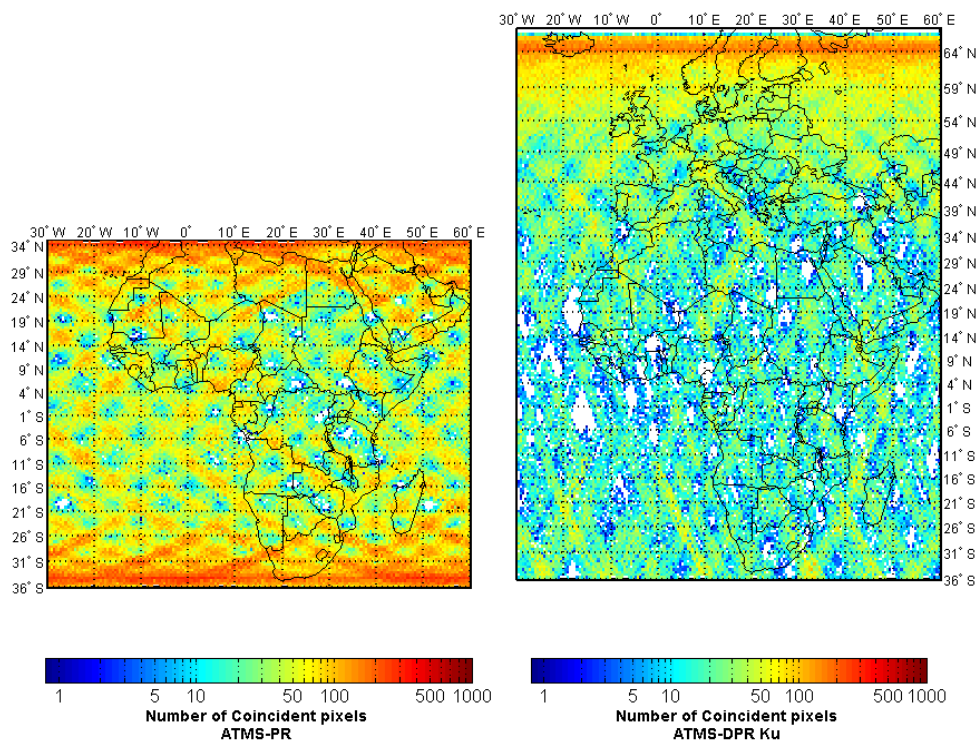


13  
 14  
 15  
 16  
 17  
 18  
 19

Figure 2 Relative sensitivity ( $S_i$ ) of the NN evaluated for five inputs ( $\Delta_{13}$ ,  $\Delta_{37}$ ,  $\Delta_{17}$ ,  $\Delta_{24}$ , LCT), for three different background surfaces.

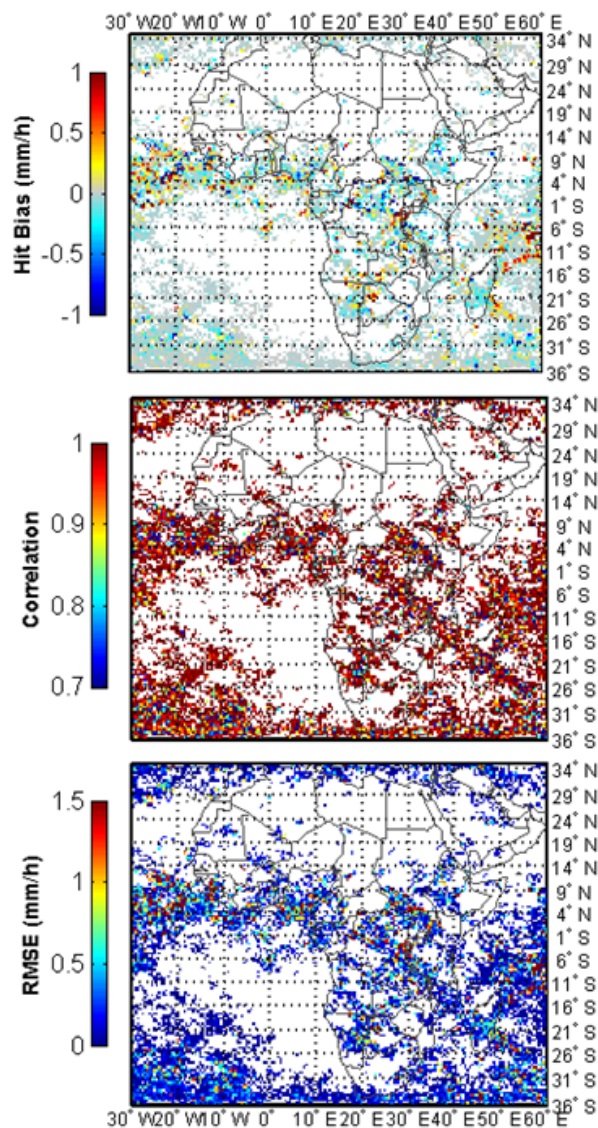


1  
2  
3



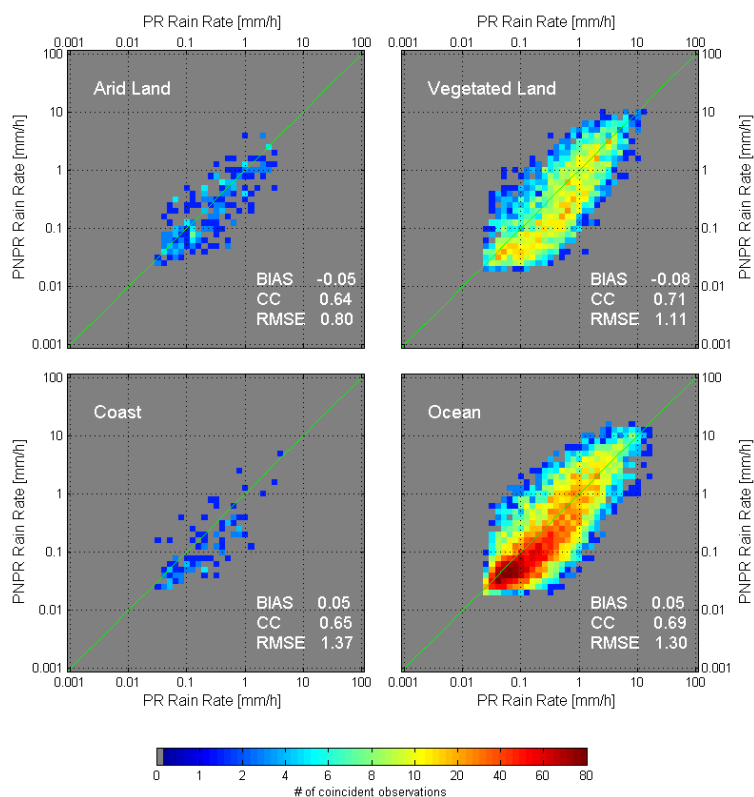
4  
5  
6  
7  
8  
9  
10  
11  
12  
13  
14  
15  
16  
17  
18  
19  
20  
21  
22  
23  
24  
25  
26  
27

Figure 3 - Number of co-located pixels from TRMM-PR and the Suomi-NPP ATMS coincident overpasses over the African area in the 24 month period 2013-2014 (left panel), and from GPM-Ku-NS and Suomi-NPP ATMS coincident overpasses over European and African areas in the 15 month period (March 2014 - May 2015) (right panel).



1  
2  
3  
4  
5  
6  
7

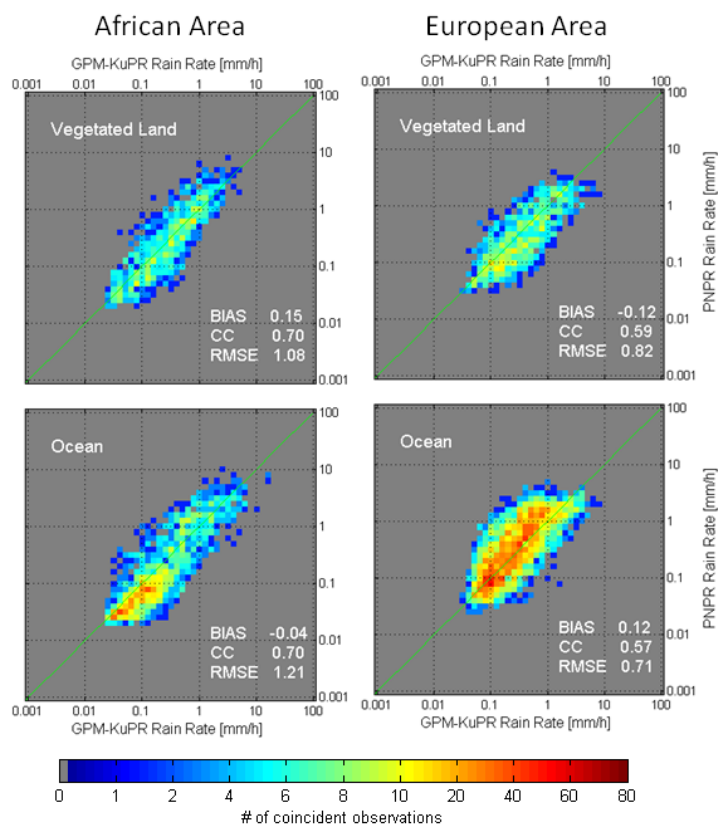
Figure 4 - Hit bias (top panel), correlation coefficient (CC, middle panel) and root mean squared error (RMSE, bottom panel), resulting from the comparison between PNPR v2 and TRMM-PR retrievals over the African area.



1  
 2  
 3  
 4  
 5  
 6  
 7  
 8  
 9  
 10  
 11  
 12  
 13  
 14  
 15  
 16  
 17  
 18  
 19  
 20  
 21  
 22  
 23  
 24  
 25

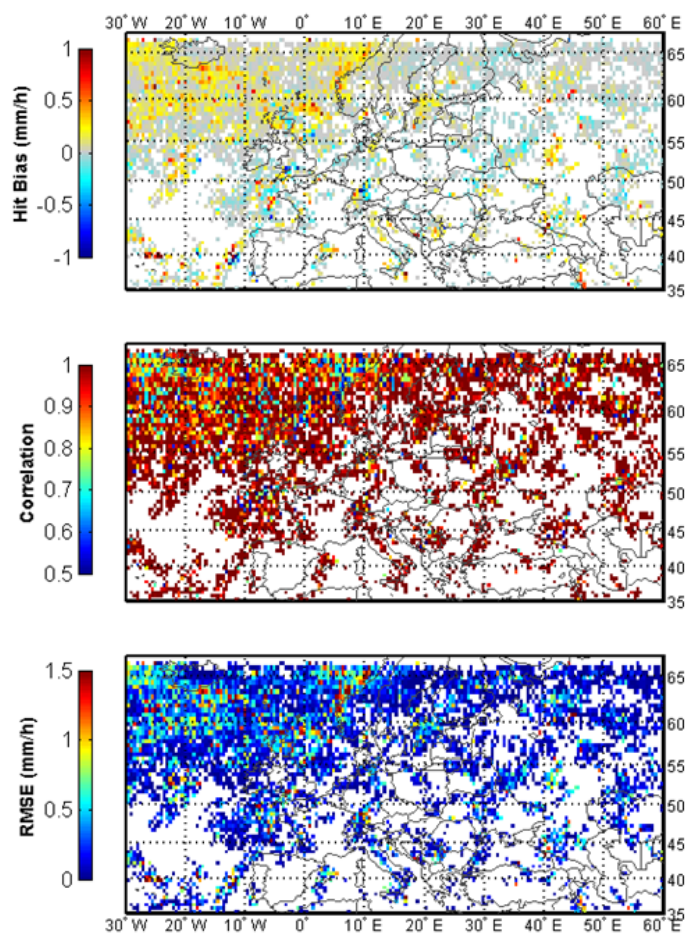
Figure 5 - Density scatterplots of the PNPR v2 and TRMM-PR mean rainfall rates (over a  $0.5^\circ \times 0.5^\circ$  regular grid), for the African area, for different surface types. A logarithmic scale is used for the precipitation rates in  $\text{mm h}^{-1}$ .





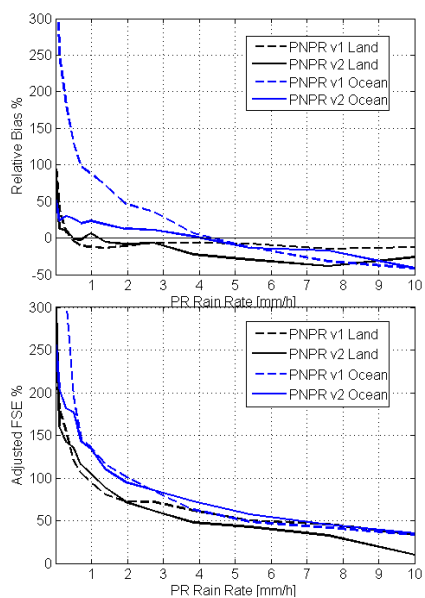
1  
2  
3  
4  
5  
6  
7  
8  
9  
10  
11  
12  
13  
14  
15  
16  
17  
18  
19  
20  
21  
22  
23  
24

Figure 6 – Density scatterplots of the PNP v2 and GPM-KuPR mean rainfall rates (over a  $0.5^\circ \times 0.5^\circ$  regular grid), for the African area (left panels), and the European area (right panels), for vegetated land and ocean. A logarithmic scale is used for the precipitation rates in  $\text{mm h}^{-1}$ .



1  
2  
3  
4  
5  
6  
7  
8  
9  
10  
11  
12  
13  
14  
15  
16

Figure 7 - Hit bias (top panel), CC (middle panel) and RMSE (bottom panel), resulting from the comparison between PNPR v2 retrievals and GPM-KuPR measurements over the European area.



1  
2  
3  
4  
5  
6

Figure 8 – Relative Bias percentage (top panel) and Adjusted FSE percentage (bottom panel), of PNPR v1 and PNPR v2 retrievals with respect to the TRMM-PR measurements.